A&A 429, 903–921 (2005)
DOI: 10.1051/0004-6361:200400035

Astronomy & Astrophysics

The G9.62+0.19–F hot molecular core

The infrared view on very young massive stars⋆,⋆⋆

H. Linz[1,2], B. Stecklum[1], Th. Henning[2], P. Hofner[3,4], and B. Brandl[5,6]

[1] Thüringer Landessternwarte Tautenburg, Sternwarte 5, 07778 Tautenburg, Germany
e-mail: [linz;stecklum]@tls-tautenburg.de
[2] Max-Planck-Institut für Astronomie, Königstuhl 17, 69117 Heidelberg, Germany
e-mail: henning@mpia-hd.mpg.de
[3] Physics Department, New Mexico Tech, 801 Leroy Place, Socorro, NM 87801, USA
[4] NRAO, PO Box 0, Socorro, NM 87801, USA
e-mail: phofner@nrao.edu
[5] Center for Radiophysics & Space Research, Cornell University, Ithaca, NY 14853, USA
[6] Sterrewacht Leiden, Niels Bohr Weg 2 (#535), PO Box 9513, 2300 RA Leiden, The Netherlands
e-mail: brandl@strw.leidenuniv.nl

Received 28 April 2003 / Accepted 28 June 2004

Abstract. We present the results of an extensive infrared study of the massive star-forming region G9.62+0.19. The data cover information from broad- and narrow-band filters in the wavelength range from 1 to 19 μm and are obtained with ESO's near- and thermal infrared camera ISAAC at the VLT and with the mid-infrared cameras TIMMI2 (La Silla, ESO) and SpectroCam-10 (Mt. Palomar). The high sensitivity and resolution provided by these facilities revealed intriguing new details of this star-forming region, especially of the embedded hot molecular core (HMC) – component F. We analyse the newly found infrared substructure of four objects in this HMC region. While one of these objects (F2) is probably a foreground field star, the nature of the brightest object in the near-infrared there (F1) remains somewhat enigmatic. Our new astrometry proves that this object is not coincident with the peak of the molecular line emission of the HMC, but displaced by ∼1.7 arcsecs which translates to nearly 10 000 AU on a linear scale. On the basis of the available data we estimate this object to be an additional embedded object with a dense dust shell. Very near the HMC location we find L' band emission which strongly rises in flux towards longer wavelengths. We presume that this emission (F4) arises from the envelope of the HMC which is known to be associated with a molecular outflow roughly aligned along the line of sight. Thus, the clearing effect of this outflow causes strong deviations from spherical symmetry which might allow infrared emission from the HMC to escape through the outflow cavities. This presents the first direct detection of an HMC at a wavelength as short as 3.8 μm. At 11.7 μm and 18.75 μm, the HMC counterpart F4 ultimately proves to be the most luminous IR source within the G9.62+0.19–F region.
In addition, within the entire G9.62+0.19 complex our narrow-band data and the K band imaging polarimetry reveal well-defined regions of enhanced Brγ and H_2 emission as well as a sector where a large contribution comes from scattered light. Combining our results with high-resolution radio data we make predictions about the extinction within this star-forming region which clarifies why some of the associated ultracompact HII regions are not visible in the near-infrared.
Our investigations show the complexity of massive star formation in its full grandeur, but they also demonstrate that the related problems can be tackled by observations using the new generation of infrared cameras.

Key words. stars: formation – stars: circumstellar matter – infrared: stars – ISM: dust, extinction – ISM: individual objects: G9.62+0.19

1. Introduction

During the last 10 to 15 years, a canonical picture of the formation of low-mass stars has been established (Shu et al. 1987; André et al. 1993), although details of the formation process are still under discussion (e.g., Hartmann 2003). On the other hand, a corresponding consistent model for the birth of massive stars ($M \geq 8$–$10\ M_\odot$) has still to be developed (see, e.g., reviews by Kurtz et al. 2000; Stahler et al. 2000; Yorke 2003). On average, sites of high-mass star formation are found at larger distances from the Sun than regions of low-mass star formation. In addition, they are located in more crowded and more heavily obscured regions than young low-mass stars are. Both facts

⋆ Based on observations made with the ESO VLT at the Paranal Observatory under programme IDs 63.I-0329 and 67.C-0264 and with ESO'S TIMMI2 on La Silla under programme ID 71.C-0438.
⋆⋆ All appendices are only available in electronic form at http://www.edpsciences.org

strongly hamper observational investigations. Furthermore, the evolution from a contracting cloud core to a high-mass main sequence star occurs on much shorter time scales, during which the protostar shows more intensive interaction with the natal environment which further increases the complexity of the problem. Thus, the requirements for studying massive star formation are severe for both the observer and the theoretician (Garay & Lizano 1999; Henning et al. 2002).

Over the last decade it has become possible to explore earlier stages in the evolution of massive young stellar objects (YSOs). While for many years ultracompact HII regions (UCHIIs) played a central role in these investigations (e.g., Wood & Churchwell 1989; Kurtz et al. 1994), recent studies have revealed that warm ($T \geq 100$ K), dense (n_{H_2} = 10^6,...,10^8 cm^{-3}) and compact (size ≤ 0.1 pc) condensations within the molecular clouds, the so-called hot molecular cores (HMCs), can provide insights into even earlier phases of the formation of high-mass stars (Cesaroni et al. 1994; Kurtz et al. 2000).

It was found that HMCs are close to, but often not coincident with, the adjacent UCHIIs (Cesaroni et al. 1994). Several authors have proposed an evolutionary scenario leading from HMCs to UCHIIs and, finally, to more evolved HII regions (Cesaroni et al. 1994; Kurtz et al. 2000).

The well-studied galactic region G9.62+0.19 (Garay et al. 1993; Hofner et al. 1996) at a distance of ∼5.7 kpc (Hofner et al. 1994) contains a number of massive YSOs in different evolutionary stages located close to each other. In this respect, there are indications that there is an age gradient from western (older) regions to eastern (younger) ones (Hofner et al. 1994, 1996; Testi et al. 1998). One of the most interesting objects of the region (source F) has been confirmed to be an HMC (Cesaroni et al. 1994; Hofner et al. 1994, 1996) by means of interferometric observations of the dense gas tracers NH_3 and CH_3CN. From high-sensitivity *VLA* measurements (Testi et al. 2000) weak cm-continuum radiation was found recently for component F, which is situated between two UCHIIs (radio components D and E).

Another feature, which makes this HMC a unique target, is the fact that very close to the location of G9.62+0.19–F emission in the 2.2 μm continuum (K band) was detected (Testi et al. 1998). According to the standard models of HMCs, in which these are described as spherically symmetric and extremely dense dust and gas spheres (Kaufman et al. 1998; Osorio et al. 1999), the optical depth should be so high that the HMC should remain undetectable at near- and mid-infrared wavelengths. This raises the question what the actual origin of the K band emission is. In this respect it is important to mention that Hofner et al. (2001) have detected a molecular outflow in G9.62+0.19 with the flow orientation very close to the line of sight, for which they favour component F as the most likely driving source. The working hypothesis of Hofner et al. (2001) was that the outflow forms a cavity of strongly decreased density roughly along the line of sight through which the infrared (IR) emission from the HMC can escape.

While the G9.62+0.19 region was covered over the years by many radio observations with ever increasing resolution and sensitivity, detailed information about this star-forming region in the infrared is rather scarce. Utilising high-resolution near- and mid-infrared data, we have explored the IR properties of this region. In Sect. 2 we explain the details of the observations we have conducted during the last four years. In Sect. 3 we present the direct results of these measurements and discuss the global features of the region and the specific properties of the HMC zone on which the emphasis of our analysis will lie. Since accurate astrometry will be a crucial issue for the following interpretation of the data, we include a detailed description of the astrometric techniques we have applied. In combination with interferometric radio maps and a radiative transfer model, we discuss the implications of our infrared data for the interpretation of the objects in the HMC region in Sect. 4. Furthermore, we compare the HMC region to the UCHIIs nearby and to the HMC in W3(H_2O). Finally, in Sect. 5 we summarise our conclusions.

2. Infrared observations

2.1. J, H, and K_s band observations

The near-infrared data were obtained in September 1999 with the infrared camera *ISAAC* (Moorwood 1997) on the *VLT ANTU* telescope within the programme ID 63.I-0329. We used the opportunity to utilise these archived data for our purposes. The following NIR broad-band filters were used: J (λ_c = 1.25 μm, $FWHM$ = 0.29 μm), H (λ_c = 1.65 μm, $FWHM$ = 0.30 μm), K_s (λ_c = 2.16 μm, $FWHM$ = 0.27 μm). The seeing conditions were between 0.65 arcsec (H-band) and 0.55 arcsec (J- and K_s-band), respectively. The pixel scale is 0.″147/px which results in a field of approximately 2.′5 × 2.′5. Within the overlap area of the 5 offset images per wavelength, the total on source integration time for each filter was 266 s . After the standard procedure (dark-field and flat-field reduction, removal of bad pixels and sky subtraction), utilising our own *IDL*[1]-based reduction pipeline for the *ISAAC* data (see also Stecklum et al. 2003; Apai et al. 2005), we corrected for the field distortion by applying the correction terms recently provided by ESO. Then the 5 dithered frames were combined to a larger mosaic image achieving subpixel accuracy. As standards for photometric calibration the stars S234–E and S071–D[2] (from the list of faint NIR standard stars by Persson et al. 1998) were observed before and after the observation of G9.62+0.19, respectively.

2.2. Br γ and H_2 observation and K narrow-band polarimetry

Images of G9.62+0.19 in the Br γ (λ_c = 2.16 μm, $FWHM$ = 0.02 μm) and in the H_2(1–)S1 (λ_c = 2.12 μm, $FWHM$ = 0.02 μm) narrow-band filters were obtained in May, 2001, again with *ISAAC* at the *VLT ANTU* telescope. Pixel scale and field of view are the same as for the JHK_s broadband imaging.

[1] Interactive Data Language.

[2] We mention here that, unlike the other finding charts shown in Persson et al. (1998), the finding chart for S071–D is (accidentally) not centred on the actual calibration star, this at first caused some confusion for our calibration.

Table 1. Summary of observations.

Date	Filter and λ_c	Telescope/Camera	FOV[a]	PSF *FWHM*	Ref. star
1999 Sep.	J 1.25 μm	ANTU/ISAAC	151″	0.″55	S234–E, S071–D
1999 Sep.	H 1.65 μm	"	151″	0.″65	S234–E, S071–D
1999 Sep.	K_s 2.16 μm	"	151″	0.″55	S234–E, S071–D
2001 May	*nb_K* 2.09 μm	"	[b] 151″	0.″65	
2001 May	H_2(1–0)S1 2.122 μm	"	151″	0.″48	
2001 May	Br γ 2.166 μm	"	151″	0.″44	
2001 Jun.	L' 3.78 μm	"	79″	0.″55 × 0.″42	HR 6070
2001 Jun.	Br α 4.07 μm	"	79″	0.″48 × 0.″41	HR 6070
2001 Jun.	*nb_M* 4.66 μm	"	79″	0.″47 × 0.″40	HR 6070
2003 Jul.	$N1$ 8.70 μm	ESO 3.6-m/TIMMI2	64″ × 48″	0.″86	HD 169916
1999 Jun.	N 11.70 μm	5-m Hale/SC-10	16″	0.″76	δ Oph
2003 Jul.	$Q2$ 18.75 μm	ESO 3.6-m/TIMMI2	64″ × 48″	1.″60	HD 187642

[a] Field of view for single frames, respectively.
[b] Imaging polarimetry with Wollaston prism and slit mask in the optical path.

The total integration times on source for both filters were 500 s within the overlap area of the 5 offset images per wavelength.

The imaging polarimetry system of *ISAAC* was used to obtain complementary NIR data for the G9.62+0.19 region. The camera is equipped with a Wollaston prism which divides the infalling light into two perpendicular polarised beams having a separation of ∼22″. The prism is used with a special slot mask (3 opaque stripes, each 20″ wide) to keep the two fully polarised copies of the imaged area separated on the detector. The first step is to simultaneously obtain the 0° and 90° data. Then, the reference plane is rotated by 45° by offsetting the image derotator of the alt-az mounting control system of the telescope accordingly. In this way, the 45° and 135° data can be obtained. To ensure a seamless coverage of the entire star-forming region, we used a 3-point dither pattern perpendicular to the stripe orientation. A narrow-band K filter was used (λ_c = 2.09 μm, *FWHM* = 0.02 μm), which does not contain strong spectral lines.

2.3. L' and M band observations

ISAAC is also capable of imaging in the L' (λ_c = 3.78 μm, *FWHM* = 0.58 μm) and *nb_M* (λ_c = 4.66 μm, *FWHM* = 0.10 μm) thermal infrared narrow bands. Within our programme 67.C-0264, service time observations were performed for G9.62+0.19 in June 2001, very shortly after the repair of the *ISAAC* chopping secondary mirror in April and May 2001. The fact that during the first weeks after recommission of the chopping mode the data were taken without field stabilisation resulted in a slightly degraded image quality, recognizable by the slightly elongated star shapes. In addition to the above-mentioned filters the 4.07 μm narrow-band filter (*FWHM* = 0.07 μm) was used which includes the Brackett α line. The pixel scale of the *ALADDIN* detector array is 0.″071/px, giving a field of view of 73″ × 73″. Since the L' and *nb_M* bands lie within the thermal infrared, on-source/off-source chopping is required to remove the thermal background in the images. Therefore we have a positive and a negative beam in the images, separated by 15 arcsec. In addition, a 5 point dither pattern was applied. The standard star HR 6070 (van der Bliek et al. 1996) was used to calibrate the data.

2.4. N and Q band observations

We utilised two different cameras to image the central region of G9.62+0.19 in the mid-infrared (MIR). The 11.7 μm image was obtained in June 1999 using *SpectroCam-10* (Hayward et al. 1993) at the 200-inch Hale Telescope of the Palomar Observatory[3]. The camera uses a 128^2 pixel Si:As BIBIB detector manufactored by Rockwell. For imaging the chip is binned into a 64 × 64 pixel array with 0.″256/pixel. The effective wavelength of the filter was 11.7 μm with a *FWHM* of 1 μm. Chopping and nodding was performed in the standard way (chopping parallel to nodding) with a throw of 20 arcsec. After applying a standard chop-and-nod reduction for the raw frames, a 5-frame mosaic was combined into the final image. The average on-source integration time at each pixel is 200 s. The star δ Oph (HD 146051) served as standard for the flux calibration.

Second, we used the *TIMMI2* camera (Reimann et al. 2000) at the ESO 3.6-m telescope for additional MIR observations in July 2003. Equipped with a 320×240 px^2 Si:As BIB *Raytheon* array, the FOV in the high-resolution mode is 64″ × 48″. Here the N1 filter (λ_c = 8.7 μm, *FWHM* = 1 μm) and the Q2 filter (λ_c = 18.75 μm, *FWHM* = 0.9 μm) have been used. The chopping and nodding throws were 15 arcsec, but both movements are performed perpendicular to each other when the TIMMI2 standard setup is used. After combination of the chopped and nodded beams the total on-source times are 749 s for N1 and 795 s for Q2, respectively. While the sky was stable and almost photometric during the N1 measurements, the Q2 band observations on the following day suffered from

[3] Observations at the Palomar Observatory were made as part of a continuing collaborative agreement between the California Institute of Technology, Cornell University, and the Jet Propulsion Laboratory.

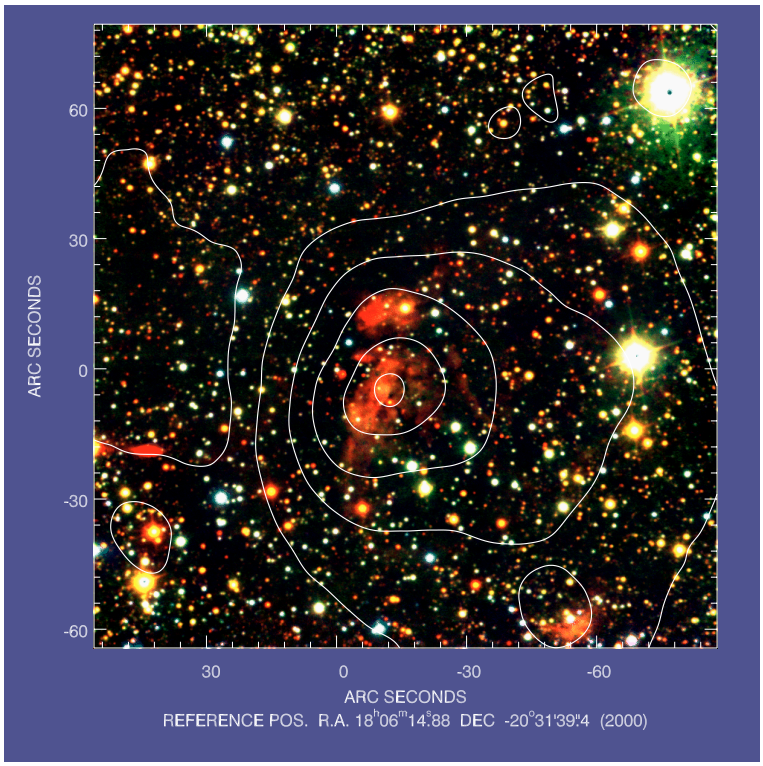

Fig. 1. Colour-coded image of the entire G9.62+0.19 region taken in the three broad-band NIR filters J (blue), H (green), and K_s (red). The large-scale contour lines denote the emission levels derived from the 8.28 μm image of the related *MSX* source. The left-most large contour line indicates the position of the close-by Infrared Dark Cloud.

mediocre atmospheric conditions. The stars HD 169916 (N1) and HD 187642 (Q2) from the list of TIMMI2 standard stars were used for calibration. We mention that the Q2 standard star was observed immediately after the end of the Q2 exposure for the science target und hence was affected by the same sky conditions.

With the *TIMMI2* data we also tried out a different (and perhaps more sophisticated) approach to create the final image, namely the so-called projected Landweber matrix restoration (Bertero et al. 2000, and references therein). We refer to Appendix C for some comments about the restoration method itself and the modifications we applied.

Because of our modified chop/nod observational approach we have to deal with artifacts (see Appendix C) in two orthogonal directions. We have undertaken the first steps to reduce these collateral effects (e.g., ghost images) by precisely aligning the array orientation along the chopping/nodding throws and by carefully registering the real values of the throws. A simple way to minimize the multiple artefacts would be, according to Bertero et al. (2000), to combine several restored images each having different throws. Due to time constraints, however, we could only perform one long integration for each filter, so we were not able to completely avoid these perturbing effects. In this respect one has to remember that a part of the original signal will still be contained in the artefacts. The effects on photometric accuracy are under investigation. For this paper we will use the restored *TIMMI2* images only to reveal the MIR morphology of the region. The photometry was always performed on unrestored and undeconvolved images.

3. Results

3.1. NIR data

In Figs. 1 and 2 we show 3-colour composites derived from the *VLT* $J - H - K_s$ data, where Fig. 2 shows the inner part of Fig. 1 in more detail and serves as a reference for the radio observation nomenclature we have adopted to indicate the various components.

Figure 1 displays the global morphology of the star-forming complex G9.62+0.19. The extended diffuse region in the centre of the image dominates the near-infrared emission and can be related to the more evolved HII component B in Fig. 2. This region harbours a cluster of modestly embedded stars. Many of them show infrared excess. Recently, Persi et al. (2003) analysed in detail this population of stars in the G9.62+0.19 B and C regions.

Eastwards of this emission, one can notice an extinction gradient. Hence, the neighbouring area, beginning a few arcsec away from the eastern border of component B, appears darker and more obscured. The superimposed *MSX* contour lines which we derived from the 8.28 μm image of the related *MSX* source (Egan et al. 1996) experience the same decrease as the NIR emission towards the eastern darker region. This is a hint for a similar behaviour of the optical depth in the near- and mid-infrared. In fact, we categorise this eastern region as a so-called Infrared Dark Cloud (IRDC – see Egan et al. 1998).

The transition strip between the two above-mentioned regions is aligned roughly along the north-south direction and is

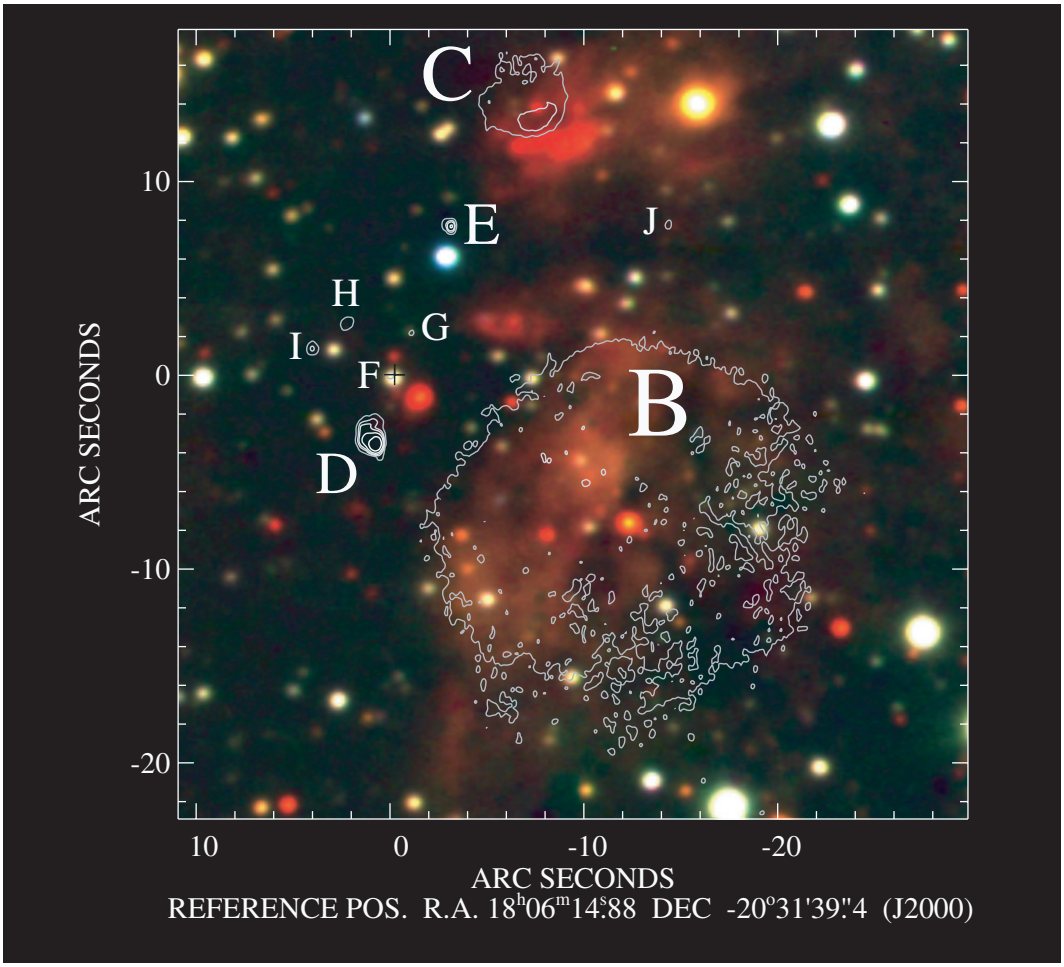

Fig. 2. Cutout of the central region of Fig. 1. The overlaid contour lines denote the 3.6 cm emission of the ionized regions as measured by Testi et al. (2000). The source annotation follows their nomenclature. Note that also component F features weak 3.6 cm emission – the related contour line merges with the seeing disk of the yellow star. The black cross marks the peak of the $NH_3(5, 5)$ HMC emission (Hofner et al. 1994).

populated with several more compact radio sources named C, D, E and F (Hofner et al. 1996; see also Fig. 2 for reference).

Mainly in the southwest of the radio component C we detect strong *K* band emission. The peak positions of the 3.6 cm and the NIR emission are clearly separated by almost 3 arcsec. This shift is obvious in Fig. 2, it is real and not an effect of an imprecise astrometry. The K narrow-band data and polarimetry data (Sects. 3.4 and 3.5) will throw light on this.

The components D and E are ultracompact HII regions (Hofner et al. 1996; Testi et al. 2000), where E might be associated either with an expanding ionised shell or with a wide-angle molecular outflow (Minier et al. 2001). Component D has a strong peak at 3.6 cm which can be recognized via the superimposed *VLA* contours in Fig. 2. Neither component shows a counterparts in our NIR data. We will discuss the consequences of these findings in Sect. 4.3.

The HMC component F was originally defined as the peak in $NH_3(5, 5)$ and $NH_3(4, 4)$ transition measurements, conducted with the VLA (Hofner et al. 1994; Cesaroni et al. 1994). The black plus sign in Fig. 2 pinpoints the peak position of this molecular line emission. (In Fig. 3 we overlay the contours of the HMC $NH_3(5, 5)$ emission onto the NIR data for comparison.) Further radio-interferometric observations revealed emission peaks in the 2.7 mm dust continuum (Hofner et al. 1996) as well as in the cm free-free continuum (Testi et al. 2000) at the position of the HMC component F. Testi et al. (1998) reported a *K*-band detection at the coordinates of the HMC. Our infrared imaging reveals an intriguing structure in this HMC region which one can decompose into at least three distinct objects. We refer to Fig. 4 for the numbering we have chosen for the objects, which will be used in this paper. On the basis of our high-resolution *VLT* data (pixel scale = 0.″15/px, seeing 0.″55) one can presume that this previous *K*-band observation of Testi (pixel scale = 0.″92/px) was suffering from the lower resolution and confusion among the objects in that line of sight which can now be clearly separated. In Appendix A we discuss in detail our approach to deriving accurate astrometry for our data.

Near the HMC peak coordinates, we find a "red" compact source according to the 3-colour-composite (object F1 in Fig. 4). However, F1 does not coincide with the hot core peak F, but is displaced by 1.7 arcsecs. Although this suggests that the compact NIR emission F1 is not a direct trace of the innermost HMC region but a distinct object we should note

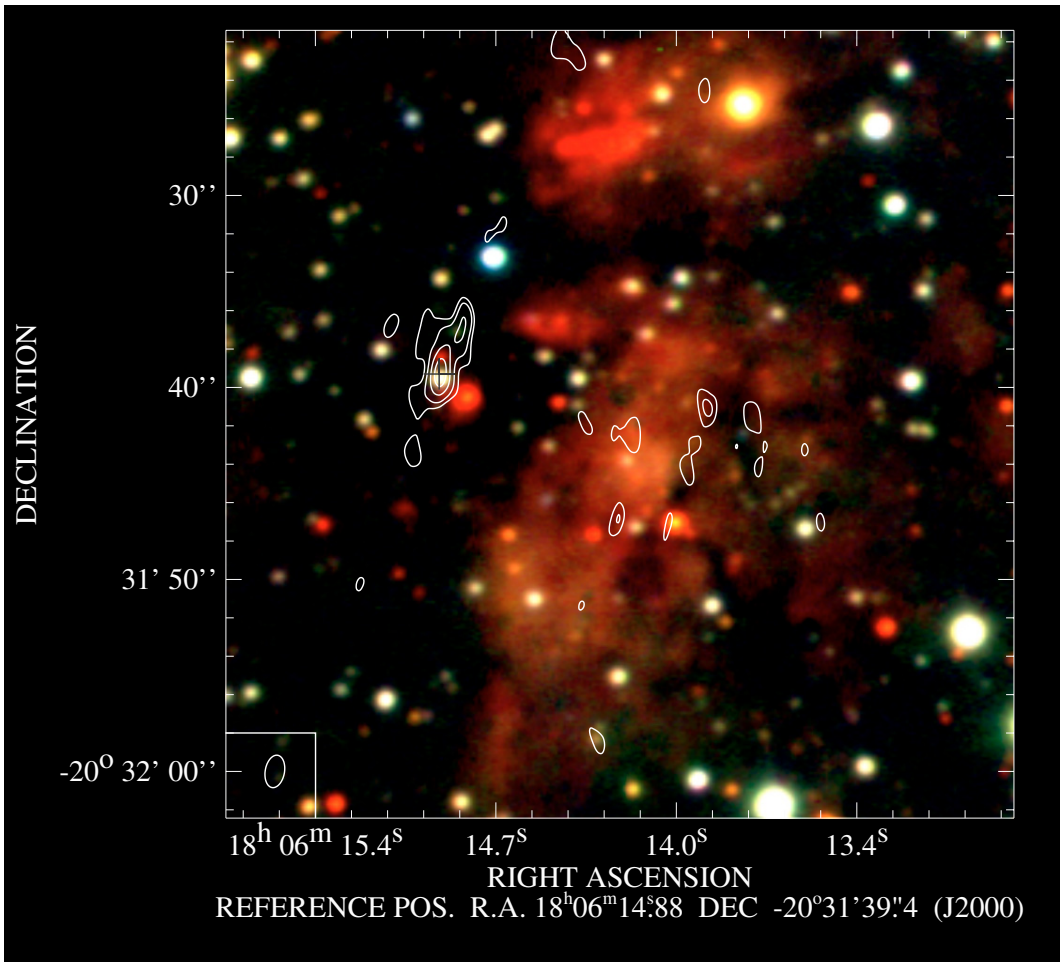

Fig. 3. The same field of view as in Fig. 2, but now the overlaid contour lines trace the thermal $NH_3(5, 5)$ emission of the HMC as measured by Hofner et al. (1994). The ellipse in the lower left corner indicates the size of the synthesized VLA beam. The black cross at the reference position marks the faint peak of the 3.6-cm HMC emission (Testi et al. 2000).

that according to Cesaroni et al. (1994) the warm ammonia emission is extended over several arcsec and a source size of 3–5 arcsec was derived. Since 1 arcsec translates to 0.028 pc (assuming a distance of 5.7 kpc) F1 might still be affected by warm and dense molecular gas of the actual HMC. Thus, we have derived the K_s band magnitude of object F1 using S234–E (K_s = 12.070 mag) and S071–D (K_s = 11.839 mag) (Persson et al. 1998) as photometric standards. By performing PSF photometry on the mosaicked science frame we derived a count rate for our object. To be in accordance with the 10″ aperture photometry applied by Persson et al. (1998) we also used this method (in form of the *MIDAS*[4] MAGNITUDE/CIRCLE routine) to derive the count rates for the standard stars. According to this procedure the F1 magnitude is K_s = 13.6 mag with 0.1 mag as a conservative error limit. Testi et al. (1998) had derived K = 12.9 ± 0.08 mag, probably for all the 3 objects visible at 2.16 μm in the F region in Fig. 4.

At the position of the HMC 3.6 cm radio peak we find another much fainter compact source (object F2 in Fig. 4). To evaluate this one should remember that this area near the IRDC is in general very extincted. It is possible to derive a preliminary extinction estimation for this region from the data contained in Schlegel et al. (1998) which results in A_λ values between 31.2 mag (J band) and 12.7 mag (K band). Therefore, other objects in the F region appear to be strongly reddened, with $(H - K)$ values clearly exceeding 1.5 mag. However, this object has a "yellow" colour index with $(H - K)$ being only 0.72 mag. By inserting the data for F2 into a $J - H - K_s$ two-colour diagram we see that the F2 colours can be explained almost completely by interstellar reddening. Therefore, we conclude that F2 is a foreground star, not physically related to the star-forming region. A definitive answer cannot be given until high-resolution NIR spectroscopy is performed with an instrument capable of resolving the objects in the HMC region (e.g., NACO on the VLT).

A third very faint source (object F3) is visible less than 1″ to the north of the foreground star. This object appears very red because it is only detected in the K_s band and not in the J or H band. Note that, according to our astrometry, an H_2O maser (the first one in the H_2O maser list in Table 2) is only 0.25 arcsec apart from the position of this object.

The photometry of the objects in the HMC region is summarised in Table 3.

[4] Munich Image Data Analysis System.

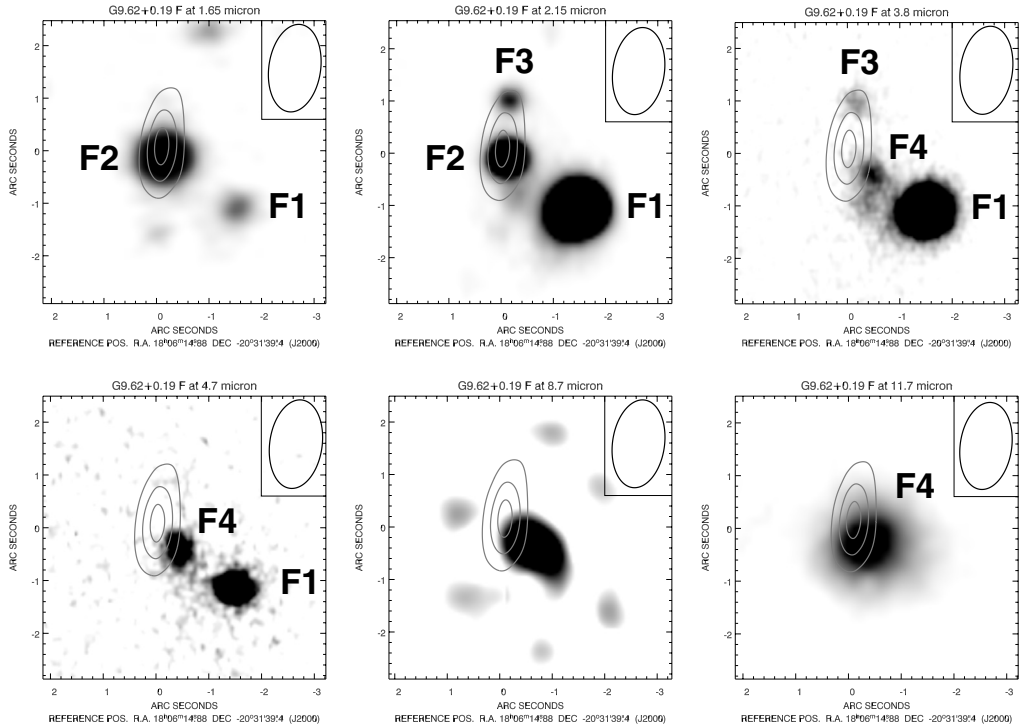

Fig. 4. Cutout gallery showing the four objects of the HMC region G9.62+0.19–F. Upper row from left to right: H, K_s, L' band. Lower row from left to right: *nb_M*, $N1$, 11.7 μm. The size of the cutout box is ca. $5\farcs4 \times 5\farcs4$. While the foreground star (F2) quickly fades towards longer wavelengths, another object very close to it (F4) gets stronger and finally dominates the region. We presume that it is a potential trace of the HMC whose location is here indicated by the upper contours of the $NH_3(5, 5)$ emission. While all the other images are taken from the plain imaging data, the $N1$ image at 8.7 μm shows the TIMMI2 data after deconvolution with the standard star HD 169916. Note that the smaller spots in that particular image are deconvolution artefacts that change their position and strength when the deconvolution parameters are varied.

Table 2. Compilation of positions of features in the HMC region.

Feature	RA(J2000)	Dec(J2000)	Telescope
$NH_3(4, 4)$	18 06 14.85	–20 31 38.91	VLA – D[(1)]
$NH_3(4, 4)$	18 06 14.81	–20 31 39.41	VLA – C[(1)]
$NH_3(5, 5)$	18 06 14.87	–20 31 39.41	VLA – C[(2)]
$CH_3CN(6–5)$	18 06 14.89	–20 31 39.20	OVRO[(3)]
2.7 mm cont.	18 06 14.89	–20 31 38.90	OVRO[(3)]
3.6 cm cont.	18 06 14.88	–20 31 39.37	VLA – BnA[(4)]
H_2O masers	18 06 14.88	–20 31 38.39	VLA – B[(5)]
	18 06 14.87	–20 31 41.21	
	18 06 14.81	–20 31 37.43	
	18 06 14.93	–20 31 41.55	
	18 06 14.86	–20 31 40.59	
	18 06 14.78	–20 31 34.71	
	18 06 14.87	–20 31 37.57	
	18 06 14.67	–20 31 31.44	
	18 06 14.98	–20 31 42.53	
Object F1	18 06 14.78	–20 31 40.48	ISAAC[(6)]
Object F2 (K_s)	18 06 14.87	–20 31 39.50	ISAAC[(6)]
Object F3	18 06 14.87	–20 31 38.39	ISAAC[(6)]
Object F4 (*nb_M*)	18 06 14.85	–20 31 39.70	ISAAC[(6)]

Ref.: (1) Cesaroni et al. (1994), (2) Hofner et al. (1994), (3) Hofner et al. (1996), (4) Testi et al. (2000), (5) Hofner & Churchwell (1996), (6) this article.

3.2. L' and nb_M band data

This wavelength range is interesting because it fills the gap between the K_s and the N band. Naturally, the signals of most of the NIR–blue field stars strongly fade and finally disappear. Hence, they do not cause confusion anymore. Still, enough objects remain in the FOV of *ISAAC* to perform accurate astrometry. Here we want to direct the attention to an interesting detail (see Fig. 4).

In the K_s band image one can clearly see the presence of three objects in the HMC region F. The "red" object F1, already mentioned in Sect. 3.1, is dominant. The object F2 which we estimated to be an unrelated foreground star is almost 1.7 arcsec away in the north-east direction. Above this we detect the third very red and weak source F3. Please note that the location of the foreground star is underlaid with weak and diffuse emission.

When we now switch to the L' band we notice that the point-like star F2 in the middle has almost totally disappeared. Instead, we now clearly see emission arising from a slightly different location, which reveals the presence of another object F4. This is evident, when we compare the relative positions of the emission centres. We mentioned the distance of 1.7 arcsec between the point-like star F2 and the "red" object F1 in the K_s band. The centre of F4 in the L' band image is clearly shifted compared to the F2 position; it is now only 1.3 arcsec away from object F1. This shift is persistent also in the 4.07 μm and the *nb_M* band image; it is a small effect,

Table 3. Measured IR fluxes in Jy (corresponding magnitudes in parenthesis) for the objects in the HMC region.

Band name	Object F1	Object F2	Object F3	Object F4
J	–	2.21×10^{-4} (17.15)	–	–
H	6.19×10^{-5} (18.00)	5.25×10^{-4} (15.72)	–	–
K_s	2.25×10^{-3} (13.60)	6.57×10^{-4} (15.00)	1.67×10^{-4} (16.49)	–
L'	2.43×10^{-2} (10.04)	–	1.00×10^{-3} (13.50)	2.95×10^{-3} (12.33)
nb_M	3.10×10^{-2} (9.21)	–	–	1.49×10^{-2} (10.01)
$N1$	1.10 (3.90)[a]	–	–	1.10 (3.90)[a]
N	–	–	–	6.00×10^{-1} (4.55)
$Q2$	–	–	–	2.28×10^{1} (–0.85)[b]

[a] In the undeconvolved $N1$ band, the objects F1 and F4 merge into one entity, whose combined flux is reported.
[b] Note that the Q2 flux is affected by a relatively large uncertainty of around 30% due to non-photometric sky conditions (see text).

but noticeable. In the following, the nature of F4 will become clearer.

3.3. N and Q band data

Figure 5 shows the central part of Fig. 1 but now at $\lambda = 11.7\,\mu$m obtained with *SpectroCam-10*. To amplify the morphological structure, we applied 25 iterations of a modified Maximum Entropy Method for noise suppression, based on the wavelet transform and developed by Pantin & Starck (1996). The extended emission coming from component B is also dominant in the mid-infrared. A second, but compact source is found near the extended B component. The accurate position and hence the correct interpretation of this compact source has been a matter of debate during recent years (cf. De Buizer et al. 2000, 2003; Stecklum et al. 2001; Persi et al. 2003). In Appendix B we describe the circumstances and explain the result of our new astrometry. We find that the compact MIR emission is coming from the HMC region, contrary to the results of De Buizer et al. (2003). We identify it with object F4 (see Fig. 4), i.e., with the HMC conterpart[5]. For a determination of the flux coming from the compact source F4, we observed the star δ Oph just before we imaged the G9.62+0.19 region. This isolated star is a strong *IRAS* source with a 12 μm flux of 149.7 Jy. Carrying out aperture photometry for the compact source (using a 3 arcsec diaphragm) and the photometric reference star, we derived a flux of (0.60 ± 0.10) Jy for F4.

The 8.7 μm N1 data proved their value especially for the MIR astrometry, as shown in Appendix B. We show these data in Fig. 6. To produce this image the matrix restoration method described in Appendix C was applied to the N1 band TIMMI2 data. Thereafter, the restored data were overlaid as contours on the NIR colour composite. As can be easily seen, they comprise a much larger field of view than the *SpectroCam-10* data in Fig. 5. We also derived the flux of the compact MIR emission at this wavelength of 8.7 μm. As is evident in Fig. 6 and Fig. 4 the emission is elongated; most of the flux stems from object F4, but object F1 might still contribute a small fraction to the total signal. We did not try to disentangle F4 and F1 and only measured the total flux with an adequately sized aperture for the photometry. One should keep in mind that the N1 filter covers a prominent PAH feature, the related emission also peaks around 8.6–8.7 μm (e.g., Peeters et al. 2002b). In fact, such PAH emission seems to be a common feature of the majority of

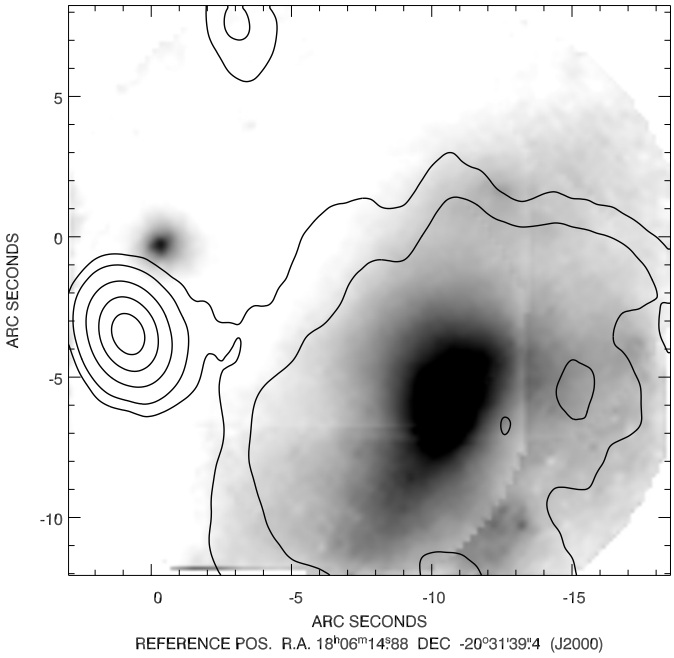

Fig. 5. Inverse gray-scale representation of the 11.7 μm SpectroCam-10 image displaying a smaller cutout of the G9.62+0.19 region. The weaker but nevertheless clearly visible spot to the east represents emission from the region of the HMC component F and arises probably from object F4 (see also Fig. 4). Overlaid are the 1.3 cm continuum *VLA* contours from Cesaroni et al. (1994). The compact radio source to the south-east of the compact MIR emission is the UCHII region G9.62+0.19 D.

[5] Persi et al. (2003) also identified the MIR source with the HMC on the basis of low signal-to-noise data and related it to the K band emission found by Testi et al. (1998). However, they apparently underestimated the significance of the multiplicity of objects in the G9.62+0.19–F region and thus could not distinguish between F1 (dominant in the K band) and F4 (dominant in the N band).

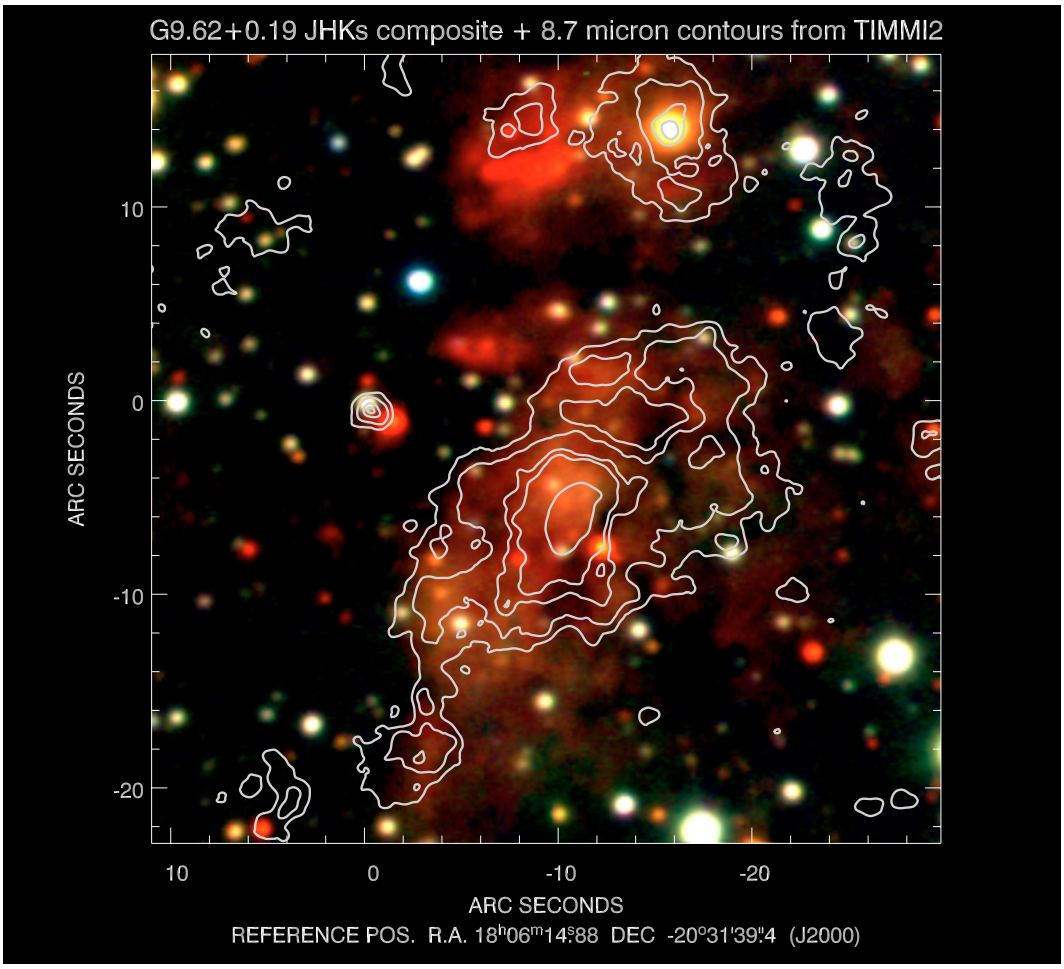

Fig. 6. The JHK_s colour composite, overlaid with the TIMMI2 $N1$ band data as contours. The bright source at the offset coordinates (−16, 14) served as main astrometric reference for the TIMMI2 data.

compact H II regions and their surroundings (Peeters et al. 2002a)[6]. Thus, the measured N1 flux is probably affected by additional contributions from those small PAHs that are susceptible to transient heating and often attain a higher (non-equilibrium) temperature than the larger normal dust grains. Indeed, the N1 flux of (1.10±0.10) Jy is higher than the 11.7 μm flux of F4.

Although the atmospheric conditions during the $Q2$ band observations at 18.75 μm were not photometric we tentatively report the measured flux of (22.8 ± 7.0) Jy for the compact emission blob we assume to be identical to F4 – no other reference objects appeared in the data except for the extended emission of component B. The quoted relatively high uncertainty of 30% is mainly caused by the non-perfect sky.

All the MIR measurements are also included in the SED plot of object F4 in Fig. 9 and draw an enlightening picture of the energetics of the HMC. In Sect. 4.1.1 we will further elaborate on the consequences of our findings for object F4.

3.4. H_2 and Brγ narrow band imaging data

In Fig 7 we combined the Br γ data (blue channel) and the H_2 data (red channel). The average of the signal of the two filters was put into the green channel. The Br γ emission of the compact HII region B clearly dominates the overall appearance of the star-forming complex. The ultra- and hypercompact HII regions D and E are not visible at all due to the large K band extinction towards these components (see Sect. 4.3 for a discussion). More interesting, the signal arising from the region of the radio C component appears almost white in this colour composite; thus, it represents just the contribution of the K band continuum without strong H_2 or Br γ line emission. We find the same for the NIR objects around the HMC region F.

The H_2 data reveal a compact emission region located between the components B and C. It appears as a flat ellipsoid with a large axis of about 5″, but it is broken up into several emission maxima and minima. This feature was also mentioned by Persi et al. (2003) and we report here the positions of the two main components according to our astrometry[7].

[6] We mention our experience with another massive star-forming region (Apai et al. 2005) where PAH emission (also covered by the MSX A band) clearly affects the SED of the central object.

[7] For the probable cause of the astrometric disagreement between our positions and the one of Persi et al. (2003) we refer to the end of Appendix A.

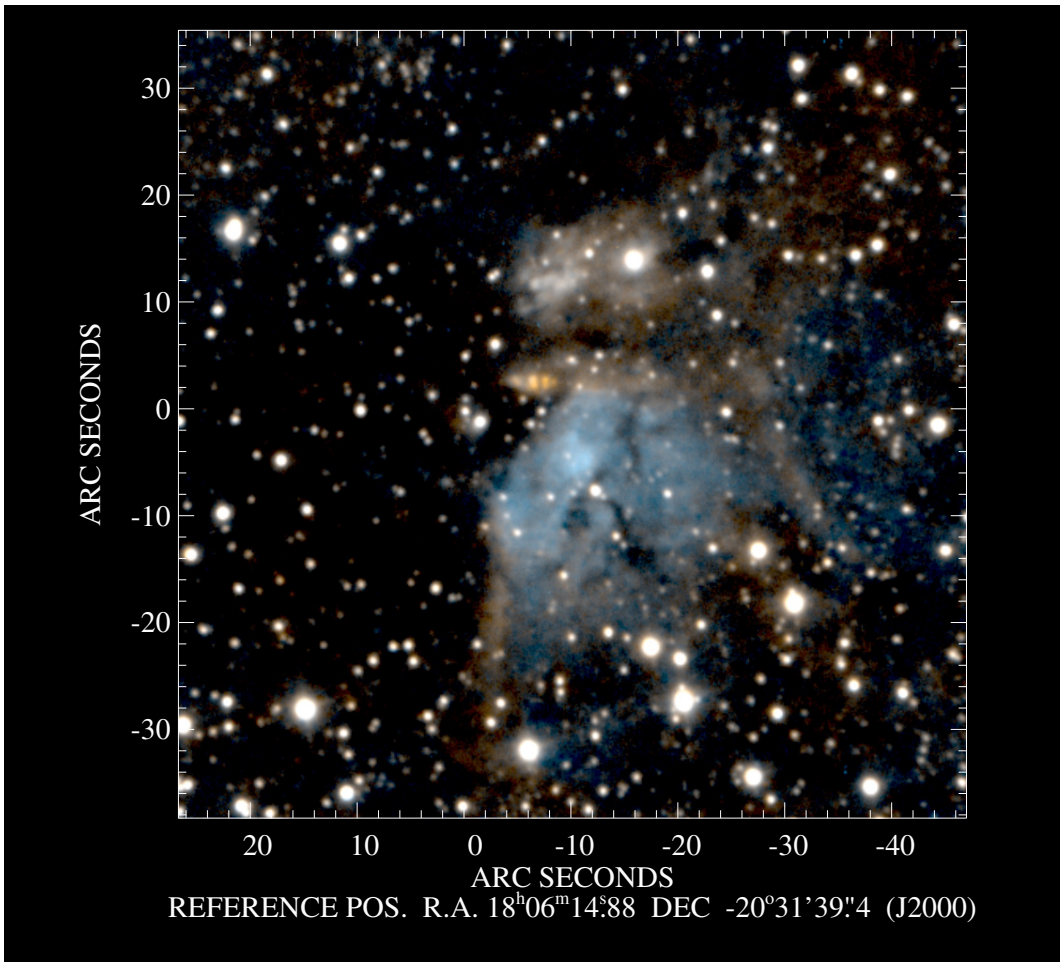

Fig. 7. This image shows G9.62+0.19 in the *K* narrow-band filters: Br γ (blue), H_2 (red), (Br γ + H_2)/2 (green). The Br γ emission arises mainly from the compact HII region G9.62+0.19 B. Note that the H_2 emission blob roughly in the image centre has its own substructure. The diffuse emission to the north of it (white) turns out to be mainly scattered light (see Fig. 8).

Component 1: $\alpha_{2000} = 18^h06^m14\overset{s}{.}42, \delta_{2000} = -20°31'36\overset{''}{.}8$; Component 2: $\alpha_{2000} = 18^h06^m14\overset{s}{.}34, \delta_{2000} = -20°31'36\overset{''}{.}8$. The projected distance to the hot core region F is roughly 7 arcsec (i.e. 0.2 pc if assuming $d = 5.7$ kpc). In principle, such a distance would allow an association with the molecular outflow arising from component F (Hofner et al. 2001). One problem is that the outflow is well aligned along the line-of-sight. Thus, if the interpretation of shock excitation due to interaction with the outflow holds, then the outflow driving source and the H_2 emission region cannot be located in the same plane of the sky, implying that the latter might be detached from the actual star-forming complex G9.62+0.19. Another possibility is the existence of another outflow in this region that was not detected in our previous studies (Hofner et al. 1996, 2001). An alternative consideration would be that a considerable fraction (if not all) of the detected H_2 emission is in fact fluorescence, excited by UV photons of the nearby HII regions (e.g., Black & van Dishoeck 1987; Draine & Bertoldi 1996, for a theoretical treatment, e.g., Fernandes et al. 1995; McCartney et al. 1999, for observational evidence for other astronomical objects). The components B or C could act as UV photon donor. Only further spectral analysis, comprising several H_2 roto-vibrational transitions, can distinguish between the collisional shock model and the fluorescence model. However, we mention that the H_2 feature is not a pure emission line object, we also see diffuse continuum emission from this position in the L' and *nb_M* band, as well as in the 2.09 μm filter used for the polarimetric imaging (see the next paragraph).

3.5. K narrow band imaging polarimetry

The polarimetric data were combined to generate a map of the linear polarisation of G9.62+0.19. We chose the standard approach for obtaining the polarimetric quantities, using the four intensities measured with the Wollaston prism (see Sect. 2.2). The Stokes parameters can be defined as:

$$Q = I(0°) - I(90°), \tag{1a}$$

$$U = I(45°) - I(135°), \tag{1b}$$

$$I = (I(0°) + I(90°) + I(45°) + I(135°))/2. \tag{1c}$$

The degree of linear polarisation ($p_{\rm lin}$) and the respective polarisation angle ($\Theta_{\rm lin}$) can then be derived by using:

$$p_{\rm lin} = \frac{\sqrt{Q^2 + U^2}}{I} \qquad \Theta_{\rm lin} = \frac{1}{2} \arctan \frac{U}{Q}. \tag{2}$$

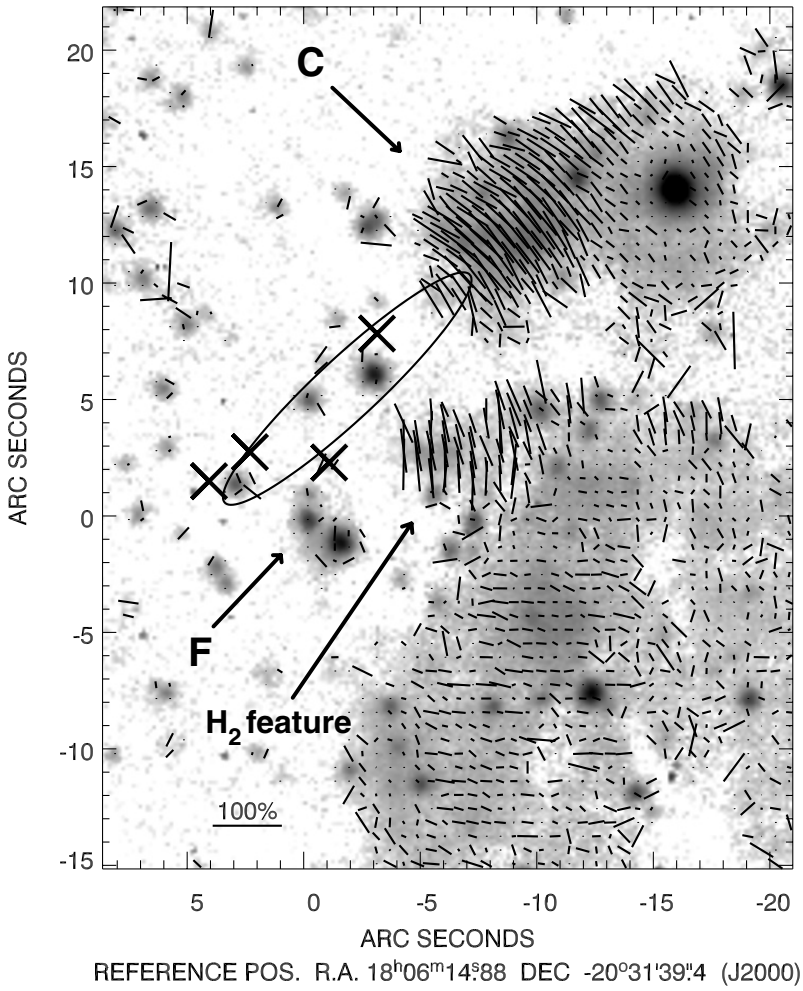

Fig. 8. Polarisation map overlaid over an image of Stokes-*I* (i.e. the intensity) of G9.62+0.19, both measured at 2.09 μm. We binned the data to a pixel size of $0\farcs6 \times 0\farcs6$ before deriving the polarisation. The ellipse is an indicator for the location of the illuminator whose scattered light causes the high degree of linear polarisation in some parts of the image (see Sect. 3.5 for details). The thick crosses mark the positions of the hypercompact HII regions E, G, H, and I (cf. Fig. 2).

In Fig. 8 we show the resulting polarisation map superimposed on the Stokes-*I* image (see Eq. (1c)) derived from the very same data set. We mention that the degree of linear polarisation as derived from Eq. (2) poses an upper limit for the true value of $p_{\rm lin}$ because of the non-standard error distribution of this quantity (e.g., Simmons & Stewart 1985). Thus, before plotting we debiased $p_{\rm lin}$ using the approach given in the appendix to the paper of Wardle & Kronberg (1974).

NIR imaging polarimetry of circumstellar matter proved to be a valuable tool for revealing the illuminating source, even in cases where it is hidden from the direct view due to enhanced extinction (e.g., Tamura et al. 1991; Yao et al. 2000; Stecklum et al. 2003). In the north-west of Fig. 8, we find two adjacent regions of strongly enhanced linear polarisation, covering the positions of component C (cf. Fig. 2) and of the H_2 emission feature (cf. Fig. 7). The debiased polarisation degree partly exceeds 50%, indicative of single-scattering events. At first glance, the arrangement of the polarisation vectors implies a common illuminator for both regions which seems to be located south-east of them towards the more obscured region of the neighbouring IRDC (see Fig. 1). The ellipse in Fig. 8 indicates the 1σ confidence region where the illuminator is probably located. It is derived by tracing the intersections of lines perpendicular to the polarisation vectors where we only took the vectors with $p_{\rm lin} > 20\%$ into account. The most probable location of the illuminator is the centre of mass (CoM) of the intersection points, whereas their distribution yields an error estimate. A 2-dimensional Gaussian is fitted to the distribution of intersection points; the computed σ parameters, which define the fitted Gaussian, are used as axes of the plotted ellipse (Weintraub & Kastner 1993; Stecklum et al. 2003). The ellipse is quite eccentric because the available polarisation vectors lie in only 2 of the 4 image quadrants. When looking carefully at the polarisation pattern one sees that the polarisation vectors related to the H_2 feature are oriented more or less north-south. Hence, when judging by eye, one would expect the centre of mass of all intersection points to be located more to the south-east of the plotted ellipse. An explanation for the different location in the plot (Fig. 8) is that we can use some 180 polarisation vectors near region C for the CoM estimation. But there are only some 30 vectors from the H_2 feature region that fulfill the conditions of sufficiently high degree of

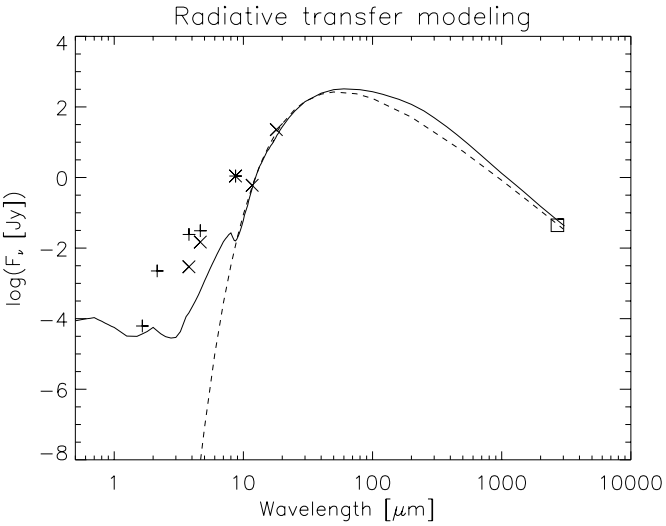

Fig. 9. Example for the appearance of the SED of a hot molecular core, calculated with a radiative transfer model (solid line). For this graph we used a central heating source with $T_{\rm eff}$ = 22 500 K and a total luminosity of 1.88×10^4 $L_\odot$. The total mass contained in the model space was 95 $M_\odot$. For this particular model we assumed a constant density distribution and an outer radius of 2600 AU. No accretion luminosity was added. The drawn-in symbols indicate the fluxes we measure for the objects F1 (plus-signs) and F4 (crosses), respectively. The asterisk at 8.7 μm denotes the integrated flux from an area covering both F1 and F4. The 2.7 mm flux from Hofner et al. (1996) is marked by a small square. As comparison, a 90 K modified blackbody is plotted as a dashed line. However, the significance of such a temperature is put into perspective in Sect. 4.1.1.

polarisation and acceptable signal-to-noise ratio in the intensity image. Thus, the polarisation vectors around component C will contribute far more intersection points than the vectors of the H_2 feature and hence will simply "preponderate" in the CoM estimation. Is this a hint that there are several illuminating sources? We mention that the error Δp is still around 8% in the high polarised regions. For ratios $p/\Delta p > 3$ the typical error for the position angle can be approximated by $28.65° \times \Delta p/p$ (Serkowski 1962). This results in an error of 4°–9° in our case. But this is of course a statistical error. It could not explain the coherent rotation of the whole polarisation pattern in one part of the image (i.e., the H_2 feature region). The bottom line of these considerations is: the observed polarisation map does not fully correspond to one coherent circularly symmetric pattern as expected in the case of only one illuminating object, thus indicating the possibility of a second illuminator.

The radio object E (Fig. 2) is situated inside the ellipse in Fig. 8 and is an illuminator candidate, at least for the scattered light near component C. However, the position of E does not really fit the polarisation pattern of the H_2 feature. We mention that the hypercompact radio components G, H, and I (Fig. 2), whose nature is not yet clarified, are located very near the 1σ confidence region for the illuminator position and their respective positions are in better agreement with the polarisation pattern of the H_2 feature. Thus, one of these sources might be responsible at least for the illumination of the H_2 feature. Since we do not see clearly corresponding NIR counterparts for these objects, they are probably deeply embedded. Should one of these objects turn out to be an illuminator, this would have implications for the distribution of its circumstellar material. A pronounced asymmetry of the ambient matter distribution would be necessary to explain how the object is able to illuminate the highly polarised regions in the K band, while we do not detect any K band emission from it in our line of sight.

The K narrow-band and polarisation data of component C prove their importance also regarding the general astrometry of the region. In Fig. 2 we see that for component C the overlaid VLA contours of the UCHII region are shifted from the NIR counterpart. One could suspect an error in the overall astrometry, if one interprets this K band emission either as arising from Br γ emission of the ionised gas and/or as thermal emission from hot dust, which usually is well mixed with the ionised gas of the UCHII region. Our data show that the Br γ fraction of the K band signal of component C is marginal and that the dominant part of this radiation probably consists of scattered light. Under these circumstances, there is no reason why the cm continuum contours should match the near-infrared emission.

4. Discussion

4.1. What is the nature of the IR objects in the HMC region?

In the previous sections we could establish the newly discovered object F4 as the actual HMC infrared counterpart by means of thermal and mid-infrared observations and careful astrometry. In this section we discuss the consequences that arise from this finding. Some more theoretical consideration will help to support our view.

4.1.1. Radiative transfer computations

To understand the properties and unusual features of the G9.62+0.19–F hot core we performed some basic continuum radiative transfer computations, utilising two self-consistent radiative transfer codes (Manske & Henning 1998; Wolf et al. 1999). For this paper we will only consider spherically symmetric models, in accordance with the standard description of hot molecular cores (e.g., Osorio et al. 1999), just to demonstrate the limitations of this concept in the case of our HMC. As input parameters we used data from Hofner et al. (1996). They had limited the spectral type of the central source to be B0.5–B1. The luminosity was estimated to be $\approx 1.8 \times 10^4$ $L_\odot$ (see also Cesaroni et al. 1994). The mass is not well constrained by other authors, but ranges between 55 and 160 $M_\odot$ (Hofner et al. 1996). Several power laws for the radial density gradient were applied ($\rho \sim r^{-\alpha}$ with α = 0.0, ..., 2.0). As grain material a mixture of silicates (Dorschner et al. 1995) and carbonaceous materials (Preibisch et al. 1993) was used. The computed fluxes comprise the range of 10^{-8}–10^{-4} Jy for $\lambda = 2.2\,\mu$m and 10^{-4}–5×10^{-1} Jy for $\lambda = 11.7\,\mu$m, respectively, and thus are at or below the detection limit of *ISAAC*, while the situation for *SpectroCam-10* at 11.7 μm is more relaxed. While parameter combinations could be found that more or less fit the

observational data points for F4 beyond 10 μm, it was not possible to also fit the data up to 5 μm.

In Fig. 9 we show the result of such a radiative transfer computation and compare it with the measured fluxes of the objects F1 and F4 mentioned in Sects. 3.1, 3.2, and 3.3. The particular parameter set used for Fig. 9 was chosen to produce preferably high fluxes in the 2–5 μm range. However, the synthetic SED should still be in accordance with the data points at longer wavelengths. For these points, the best fit was reached with a constant density distribution, an outer radius of 2600 AU, a total luminosity of 1.88×10^4 $L_\odot$, and a dust mass of 0.94 $M_\odot$ inside the model space (see Fig. 9). The optical depth for this particular configuration was $\tau_v = 673$. It becomes evident that the F4 emission in the 2–5 μm range is still more than an order of magnitude stronger than predicted by the model. We interpret this as support for the idea that spherical symmetry is not applicable in the case of G9.62+0.19–F. However, a comprehensive two-dimensional modelling of the observed fluxes would be beyond the scope of this paper.

To guide the eye, we added in Fig. 9 a modified blackbody curve to the radiative model SED that also fits quite well the data points at longer wavelengths. The effective temperature of such a modified blackbody would be 90 K, the wavelength dependence of the opacity is described by $\kappa_m \sim \lambda^{-1.0}$ in our case. However, the significance of such a temperature estimation is questionable for the object class of HMCs. As shown, e.g., by Yorke (1980) and Yorke & Shustov (1981), the concept of an effective temperature and an effective radius is not well defined for very dense dusty envelopes around protostellar objects, they can strongly deviate from the blackbody or greybody nature. Furthermore, we should note that such an effective temperature might be misleading in the following regard. It was shown by means of simple radiative transfer considerations, e.g., by Schreyer et al. (1996) that the mass-averaged dust temperature, i.e. the temperature averaged over density and particle size distribution, is always lower (ΔT = 15,..., 30 K) than the theoretical colour temperature derived from the SED for dense shells around massive YSOs. Thus, most of the mass in such a shell will attain a clearly lower temperature than implied by the colour temperature. This is important when using a temperature to derive dust masses from infrared or mm observations.

The estimated luminosity of 1.88×10^4 $L_\odot$ from our simple model is in good agreement with previous predictions (Cesaroni et al. 1994). When we also take into account the measured excess flux of F4 at shorter wavelengths (in comparison to the radiative transfer models and the modified blackbody approximation) we gain another 1000 $L_\odot$. Hence, the entire luminosity is approximately 20 000 $L_\odot$. This seems to prove that the HMC in G9.62+0.19–F indeed harbours a young high-mass star. However, caution is advisable, as we see in the case of the Orion Hot Core, where on a much smaller scale than in our case several infrared sources can be distinguished (Dougados et al. 1993), and the discussion about the energy budget of the individual sources has not settled yet (e.g., Gezari et al. 1998, 2003).

4.1.2. Hints from the polarimetry

The polarimetric data can provide additional information on the geometry of the observed regions. In a scenario where an outflow has opened the dense molecular shell of a molecular hot core, infrared radiation can escape through a channel of reduced density. The light will be scattered at the cavity walls ("dust mirroring") which represent an increased column density of scatterers in the optically thin cavity environment (Yao et al. 1997, 2000). These single scattering events can lead to high degrees of linear polarisation (e.g., Fischer et al. 1996). Hence, we would expect to perceive a clear increase of NIR polarisation.

In contrast, the measured polarisation for object F1 is relatively low (10 ± 5)%, especially when it is compared to polarisation degrees in its immediate vicinity[8]. There, the polarisation increases up to (33 ± 10)% in the small region of diffuse emission to the southwest of F2, but not including F2 or F1 (best to be seen in the 2.16 μm image of Fig. 4 at the offset position (–0.3, –0.8). Based on the low-resolution NIR imaging of Testi et al. (1998), we suggested in our recent outflow paper (Hofner et al. 2001) that object F1 itself represents infrared emission arising from the HMC region which might be cleared in parts by the molecular outflow. Taking our high-resolution infrared data, the improved astrometry and the results of the polarimetry into account, we no longer believe that this model can satisfactorily explain the properties of object F1.

However, this scenario is certainly a good interpretation for the diffuse emission behind the foreground star. It appears unlikely that this diffuse emission is just the result of the reflection of light coming from the foreground star F2. In such a case of backscattering the reflected light should more closely resemble the colour behaviour of the illuminating star. Moreover, there should be a tendency for a slighly more bluish SED of the backscattered light due to the decreasing scattering efficiency for increasing wavelengths. This is not observed. Instead, the diffuse emission is clearly redder than the star and seems to be associated with object F4 whose emission strongly increases in the L' and *nb_M* band, while the star F2 strongly fades beyond 2.2 μm. We therefore think that this star F2 is clearly detached from the actual star-forming region.

We should re-emphasise that both the weak cm continuum emission and the $NH_3(5, 5)$ emission associated with the HMC component F peak very close ($\leq$0.″4, cf. Table 2) to F4 (see also Figs. 2 and 3) which suggests an intrinsic entanglement of the two components. Thus, we interpret F4 as arising from the inner parts of the HMC outflow cavity.

One detail is not yet clarified: is the L' and *nb_M* band signal of F4 caused by direct thermal dust emission of hot grains very near to the embedded power source of the HMC? Or can a considerable fraction of the overall emission be attributed to reprocessed light scattered on the cavity walls? In the latter

[8] It is difficult to confirm this claim just by looking at Fig. 8. This kind of plot is well-suited for visualising the polarisation pattern for extended emission but is often misleading around compact sources with steep intensity gradients. In these cases the polarisation has to be derived by aperture photometry centred on the compact sources in all the polarimetric frames and then applying Eqs. (1) and (2).

case one has to assume the existence of larger dust grains in the HMC envelope to ensure a reasonably high scattering efficiency[9] for wavelengths of 3–5 μm.

These ideas about larger grains are more than a wild speculation. Grain growth is expected to occur in YSOs and their near vicinity, in particular in circumstellar disks (e.g., Beckwith & Sargent 1991; Beckwith et al. 2000; D'Alessio et al. 2001). Recent observations (e.g., McCabe et al. 2003; Shuping et al. 2003) seem to indicate – cum grano salis – the existence of a considerable amount of micron-sized particles in disks around low-mass YSOs. Systematic investigations of massive YSOs seem to be scarcer, especially regarding HMCs. However, for the best-known region of ongoing massive star formation, Orion, polarimetric observations at 2.2 and 3.8 μm point to the existence of larger grains in the Orion Molecular Cloud in general (Rouan & Leger 1984) and in particular in the BN/KL region containing the Orion Hot Core (Minchin et al. 1991; Dougados et al. 1993).

Thus, a future task will be to conduct high-resolution polarimetric measurements in the K, L', and *nb_M* band. Adaptive optics systems like *CONICA/NAOS* at the VLT seem to be most suitable to ensure high resolution (0.″1) combined with high sensitivity – characteristics that are absolutely necessary for delivering meaningful polarimetric results in the case of G9.62+0.19–F.

4.1.3. Ordinary stars within the HMC vicinity?

We have already pointed out that object F2 very near the HMC is probably a foreground star. Is it also possible that object F1 is a normal star whose photospheric emission we see? We have several reasons for rejecting this possibility.

We start with the following estimate: we use the well-known correlation between the colours of a star and its colour excess due to additional reddening:

$$H - K = (H - K)_0 + E_{H-K}. \quad (3)$$

Herein, $(H-K)_0$ is the unreddened intrinsic colour of the star and the colour excess E_{H-K} can be expressed as

$$E_{H-K} = A_H - A_K = \left(\frac{A_H}{A_K} - 1\right) A_K. \quad (4)$$

According to Mathis (1990), the A_H/A_K ratio for the standard interstellar reddening law ($R_V = 3.1$) is around 5/3. We can use the intrinsic stellar colours (e.g., Wegner 1994, for O and B stars; Bessell & Brett 1988, for stars of type A–M) and our measured value $H - K = 4.4$ mag to derive the K band extinction A_K. O stars of all luminosity classes have $(H-K)_0$ values between −0.08 mag and −0.02 mag. In combining Eqs. (3) and (4) we find that A_K is always larger than 6.6 mag for our case. Together with the distance modulus of 13.8 (assuming $d = 5.7$ kpc) and the measured K band magnitude of 13.6 mag (see Table 3), the absolute K magnitude M_K would be −6.8 mag. Moreover, if we take into account that all O stars have $(V-K)_0$ values between −0.7 mag and −0.9 mag, the absolute visible magnitude M_V would be brighter than −7.5 mag! O and B stars do not feature such bright M_V values, only very extreme supergiants (luminosity class 1a-0) would exhibit such a characteristic. Furthermore, if we considered late-type giants we would also have to deal with extreme luminosity classes which, in addition, would cause a severe dilemma in explaining the existence of a very old star almost in the centre of a young star-forming region.

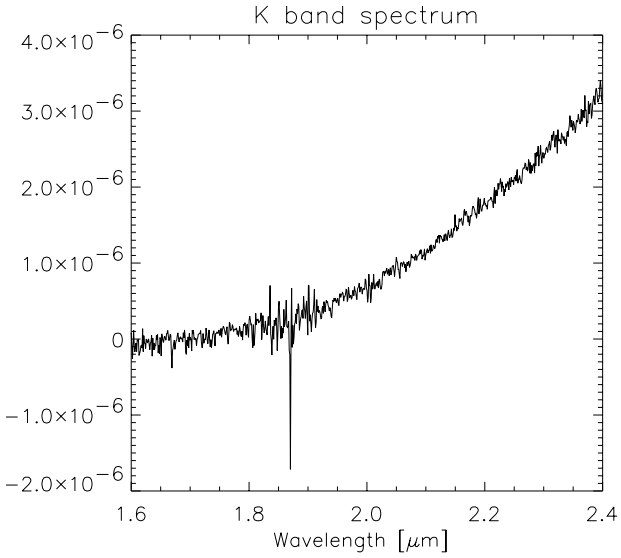

Fig. 10. The K band medium-resolution spectrum of object F1 (in arbitrary units), taken with SOFI at the ESO NTT.

Striking evidence against photospheric emission comes from the K band medium-resolution spectrum (Fig. 10) which was taken with SOFI at the 3.5-m NTT on La Silla, Chile (Testi 2001). The slit was centred on the object F1, but the spectrum probably also covers some contribution from the foreground star F2. Around 1.87 μm the transmission of the atmosphere strongly decreases due to strong H_2O absorption, separating the near-infrared H and K band. The strong feature around 1.87 μm probably arises from the fact that this atmospheric imprint was not totally canceled out in the calibration. In the range between 1.95 and 2.40 μm we see a spectrum without prominent features. Especially late-type stars with their relatively cool atmospheres should show many metallic lines and even molecular lines. A characteristic feature for such stars are more or less strong CO absorption features between 2.29 μm and 2.40 μm (Ramirez et al. 1997; Bieging et al. 2002), but we only see an almost featureless spectrum monotonically rising towards the K band edge, which is an imprint of continuum dust emission.

These points speak clearly against the "naked star" interpretation for the object F1. They rather indicate the presence of an embedded object within a dusty shell. In a way, this resembles the situation of the Orion BN/KL region where several IR objects are located in the vicinity of the Orion Hot Core. It might be tempting to see our object F1 as an analogue to

[9] Usually, the scattering efficiency is strongly diminished at wavelengths beyond ≈2−3 μm when only dust is considered with the standard MRN size distribution (Mathis et al. 1977) typical for the interstellar medium, i.e., the overwhelming majority of the dust particles is sub-micrometer-sized with a typical diameter of ≈0.1 μm.

the BN object with regard to the general appearance and the dusty shell nature of both objects. However, this analogy does not hold. Figure 9 indicates that F1 reaches its maximum emission at a wavelength around 5 μm and then drops again and hence is not detected at 11.7 μm anymore. This suggests an object of lower luminosity (a few tens $L_\odot$, if really located at d = 5.7 kpc). BN is 70–100 times more luminous than F1 (1500–2500 $L_\odot$; Dougados et al. 1993; Gezari et al. 1998), it has probably a far more massive reservoir of dust around and is of course still strong at 10 and 20 μm.

4.2. Comparison with other HMCs

To date, the number of firmly established HMC sources is still quite small. Apart from the well-investigated Orion BN–KL region, only a few HMCs have been studied by means of high-resolution infrared observations (cf. Stecklum et al. 2001, 2002; De Buizer et al. 2002, 2003; Pascucci et al. 2004).

In this respect, it is worth comparing the infrared properties of our region with a similar examination of the hot molecular core in W3(H_2O). Both HMC regions seem to be related to outflow activity. But in the latter case no NIR/MIR emission could be detected in the direct vicinity of the HMC (see Stecklum et al. 2002). One explanation could be that the outflow is mainly in the plane of the sky, so that we cannot benefit from an outflow-related clearing effect.

Another possibility might be that the potential outflow material had not yet have time enough to sufficiently penetrate the very dense shell of the inner HMC region as is instead apparently the case for our HMC component F. In that case, we would rate the G9.62+0.19 hot molecular core to be in a more evolved state than the W3 one.

Support for this argumentation comes from recent 3-mm and 1.3-mm interferometric line observations of G9.62+0.19 with OVRO (Liu 2003). This author discusses the use of several molecules as chemical clocks. First, he uses H_2S to re-confirm the age differentiation among the components D, E, and F, since H_2S is eventually transformed into other species after it has been liberated from grain mantles into the warm molecular core environment. Among the three cores, component F shows the highest H_2S abundance and would thus be younger than E and D both of which have already developed an ultracompact HII region. This finding is in accordance with our previous results of the NH_3/CH_3CN abundance comparison (Hofner et al. 1996). Furthermore, Liu (2003) compares the CH_3OH and C_2H_5CN emission at 3 mm. While the observed methanol emission shows extended structure along the molecular ridge including D, E and F, ethyl cyanide is primarily detected toward core F. Since revised chemical HMC models usually produce significant amounts of N-bearing molecules only after O-bearing species have reached their peak abundances (e.g., Rodgers & Charnley 2001, 2003), the strong C_2H_5CN emission toward component F suggests that it is in a more advanced stage of HMC evolution.

This fits well to the scenario advocated by Kurtz et al. (2000) that HMCs can evolve first into hypercompact (Gaume et al. 1995; Tieftrunk et al. 1997; Kurtz 2000) and finally into ultracompact HII regions. The detection of weak emission at 1.3 and 3.6 cm, associated with a high emission measure of 3×10^8 pc cm^{-6}, by Testi et al. (2000) implies that the HMC component F is on its way to cultivate a hypercompact HII region.

Furthermore, Cesaroni et al. (1998) analysed two other well-known hot molecular cores (G10.47+0.03 and G31.41+0.31) and found indications that the HMC stage marks the phase of transformation from spherically symmetric to flattened and non-spherical structures. Also in this regard, G9.62+0.19–F proves to be a typical example of an HMC.

4.3. Why can't we see the D and E components in the infrared?

Radio component F which is only a weak cm continuum source nevertheless shows infrared features in its immediate vicinity. Hence, at first glance it might be intriguing that the stronger radio sources D and E, which both are more massive and energetic than component F (Hofner et al. 1996), do not show an infrared counterpart. Without a further analysis one might come to a similar conclusion as De Buizer et al. (2000) who, for lack of exact astrometry, just shifted their mid-infrared source to the position of the radio D component. To clarify these circumstances, we reconsider radio data from previous papers about G9.62+0.19 to derive the expected Brackett γ fluxes from, as well as the extinction towards, D and E.

4.3.1. The expected Br γ fluxes of D and E

The method to compute the expected flux in IR recombination lines on the basis of cm continuum data has been explained extensively by Watson et al. (1997) and was also applied in some of our previous investigations of other massive star-forming regions (e.g., Feldt et al. 1998, 1999). We refer to these papers for details and start with their formula for the emission measure (EM), which can basically be derived from the approximation of Altenhoff et al. (1960) for the optical depth of cm free-free emission:

$$EM = 4.72\ a^{-1}\ T_{\rm e}^{1.35}\ \nu^{2.1}\ \ln\left(\frac{T_{\rm e}}{T_{\rm e} - T_{\rm b}}\right) {\rm cm}^{-5}. \quad (5)$$

Herein, $T_{\rm e}$ and $T_{\rm b}$ are the electron temperature and the brightness temperature, respectively, both in Kelvin. The parameter ν is the frequency (in Hz) at which $T_{\rm b}$ was derived. Finally, $a(\nu, T)$ is a correction factor of the order of 1, which is tabulated in Mezger & Henderson (1967) for various frequencies and electron temperatures[10].

By adopting the approach of Osterbrock (1989) we can use the emission measure to compute the expected Br γ flux under the assumption that no extinction occurs:

$$S_{\rm Br\gamma} = 0.9\ h\nu_{\rm Br\gamma}\ \alpha^{\rm eff}_{\rm Br\gamma}\ \frac{\Omega_{\rm Br\gamma}}{4\,\pi}\ EM. \quad (6)$$

[10] Beckert et al. (2000) demonstrate that this approximation (Altenhoff + Mezger & Henderson correction factor) is in very good agreement with non-approximative numerical solutions up to frequencies of ~100 GHz.

Table 4. Physical parameters of the radio components D and E.

Physical parameter	Component D	Component E	Extinction law[b]
T_b [K] [a]	977	210	
T_e [K]	8000	8000	
N(H) [cm^{-2}]	2.54×10^{24}	1.84×10^{24}	
$S_{Br\gamma}$ [W cm^{-2}]	1.083×10^{-19}	2.21×10^{-20}	
$A_{2.2\,\mu m}$ [mag]	125	90	$R_V = 3.1$, $CF(2.2\,\mu m) = 0.108$
$A_{12\,\mu m}$ [mag]	32	23	$R_V = 3.1$, $CF(12\,\mu m) = 0.028$
$A_{2.2\,\mu m}$ [mag]	232	168	$R_V = 5.0$, $CF(2.2\,\mu m) = 0.125$
$A_{12\,\mu m}$ [mag]	60	43	$R_V = 5.0$, $CF(12\,\mu m) = 0.032$

[a] The brightness temperatures were derived taking the emission in the inner 0.″55 of the components into account which corresponds to our K_s band resolution element (i.e. seeing).
[b] See Sect. 4.3.2 for details.

The factor 0.9 reflects the assumption that a UCHII region consists of ∼10% of singly ionised helium, which contributes electrons *and* ions to the cm free-free emission but only electrons to the Br γ emission. For $\alpha^{\rm eff}_{Br\gamma}$, which comprises the transition coefficients and the level populations via a temperature dependency, Hummer & Storey (1987) give:

$$\alpha^{\rm eff}_{Br\gamma} = 6.48 \times 10^{-11}\, T_e^{-1.06}. \quad (7)$$

For our computations we derived the brightness temperatures of components D and E from the 1.3 cm map of Testi et al. (2000)[11]. The electron temperatures of both regions were estimated by Hofner et al. (1996), using a thermal bremsstrahlung model to fit the cm continuum observations conducted up to that point. We list all the parameters in Table 4.

The expected Brγ flux is 1.083×10^{-19} W cm^{-2} for component D and 2.21×10^{-20} W cm^{-2} for component E for the theoretical limit of zero extinction. These values correspond to 5.75 mag and 7.48 mag in terms of K band magnitudes. If we use the ISAAC camera in combination with the Brγ filter, we would detect such fluxes with an SNR of 20 within less than 1 s of exposure time.

4.3.2. The extinction towards D and E

To evaluate these numbers one has to estimate the extinction towards these regions. Hofner et al. (1996) derived H_2 column densities, based on interferometric $C^{18}O(1–0)$ observations, for the components D, E, and F. They report values of $N(H_2) = 12.7 \times 10^{23}$ cm^{-2} for component D and $N(H_2) = 9.2 \times 10^{23}$ cm^{-2} for component E. To transform these column densities into extinction values we start with the empirical relation that links the total hydrogen column density N(H) to the optical colour excess E_{B-V} (Ryter 1996):

$$N(\mathrm{H}) = 6.83 \times 10^{21}\, E_{B-V}\ \mathrm{cm^{-2}\ mag^{-1}}. \quad (8)$$

In order to substitute E_{B-V}, we use the ratio R_V of absolute to relative extinction:

$$R_V = A_V \,/\, E_{B-V}. \quad (9)$$

Combining Eqs. (8) and (9) we get an expression for the visible extinction A_V, based on column densities. Finally, we can introduce a conversion factor $CF(\lambda)$ that represents the conversion from the visible extinction (A_V) to extinction values at other wavelengths (A_λ). We arrive at the following expression:

$$A_\lambda = \frac{R_V\ N(\mathrm{H})}{6.83 \times 10^{21}\ \mathrm{cm^{-2}\,mag^{-1}}}\ CF(\lambda). \quad (10)$$

Mathis (1990) gives two sets of conversion factors, corresponding to two possible extinction laws: normal "diffuse interstellar dust" ($R_V = 3.1$) or "outer-cloud dust" ($R_V = 5.0$). For both possibilities, we compute extinction values at 2.2 μm and 12 μm using $N(H) = 2 \times N(H_2)$. The results are listed in Table 4. In any case, the extinction is ≥90 mag at 2.2 μm and still ≥23 mag at 12 μm. Such a large extinction would attenuate the fluxes down to an undetectable value. But one important restriction applies to this "naïve" interpretation of the extinction data. The $C^{18}O$ line is optically thin; hence, it traces the column density of the whole molecular cloud and not just the column density up to the UCHII regions. Theoretically, the UCHII regions could even be located in front of the molecular clouds, which is obviously not the case.

4.3.3. Relative positions of UCH II regions and the molecular gas

One approach to clarifying the situation is to compare the LSR velocities of radio recombination lines (RRLs) produced

[11] The 3.6 cm map of Testi et al. (2000) has a higher SNR, but Hofner et al. (1996) found that the behaviour of the components D and E already deviates from the optically thin regime at this wavelength.

in the UCHII region with the LSR velocities of molecular lines seen in absorption against the radio continuum of the UCHII region. This idea has already been pursued by Downes et al. (1980) and was recently revived by Araya et al. (2002) who could show that in almost all of their UCHII region targets the ionised gas and the main absorbing molecular component have the same velocity within the uncertainties of the measurements. This demonstrates that a close association between the two classes of objects is very common.

1.) As far as we know, no radio recombination line studies exist for G9.62+0.19 that would provide high spatial resolution. Therefore, we go back to the seminal work of Downes et al. (1980) who conducted a combined survey of the H110α RRL and H_2CO ($1_{10}-1_{11}$) absorption line with the Effelsberg 100 m telescope at 6 cm. Their observations for G9.62+0.19 were centred on component B and had a half-power beamwidth of ~2.6 arcmin. The reported LSR velocities are (3.0 ± 5.0) km s^{-1} for the RRL and (2.0 ± 0.5) km s^{-1} for the H_2CO absorption line[12]. The velocities are almost equal which speaks for a close association also in the case of G9.62+0.19;
2.) the fact that we actually see absorption implies that a noticeable fraction of the molecular gas is located in front of the HII regions;
3.) the measured H_2CO line temperature for G9.62+0.19 is smaller than the continuum temperature of the ionised sources (Downes et al. 1980). An opposite finding would imply that most of the H_2CO absorption occurs just by absorbing photons of the Cosmic Microwave Background and would therefore not be related to the HII regions at all;
4.) in our HCO^+ data of G9.62+0.19 (Hofner et al. 2001), which we took with the IRAM 30 m telescope and with the Plateau de Bure (PdB) interferometer, we clearly see a strong absorption dip in this molecular line at the LSR velocity of the RRLs and the H_2CO absorption. An interpretation we mentioned in the paper is self-absorption due to a high optical depth. However, this feature can also be understood as absorption against the 89 GHz continuum of the (ultra)compact HII regions. Probably both effects contribute to the observed line absorption. Note that the PdB data provide sufficient spatial resolution to distinguish between components D and E and that component B is not dominant in these data;
5.) regarding the morphology of the components D and E we do not see features that could explain these UCHII regions within the scope of blister/champagne flow models (Tenorio-Tagle 1979; Yorke 1986) which would be the consequence of the location of the UCHII regions very near the border of the embedding molecular cloud.

These five points support the idea that both cm continuum components (D and E) are clearly embedded within their parental molecular cloud, although we cannot exactly estimate their relative positions. We cite here recent investigations by Kim & Koo (2003), based on molecular line observations towards 16 UCHII regions. They indicate that the formation of massive stars, in general, does not take place near the surface of molecular clouds but in their interiors. In this regard, one has to take into account that already the positioning of the UCHII regions D and E behind 20% of the total amount of molecular gas would be sufficient to explain our non-detections. On the basis of these considerations we conclude that the invisibility of the components D and E in the near- and mid-infrared is a reasonable finding.

[12] The RRL velocity is confirmed by Lockman (1989) who gives v_{LSR} = (4.1 ± 0.8) km s^{-1} for the H85α, H87α and H88α lines towards G9.62+0.19, based on observations with the NRAO 43 m telescope with a *FWHP* of 3 arcmin.

5. Conclusions

We have performed a comprehensive set of infrared observations for the G9.62+0.19 star-forming region. Narrow-band and broad-band observations from 1 to 19 μm provided new information about this complex of young stellar objects. In the following we summarise our results.

1.) The high resolution of our data revealed the detailed structure of the Hot Molecular Core region G9.62+0.19–F. The *K* band emission found by Testi et al. (1998) could be disentangled into three distinct objects. Our astrometry shows that among these three objects the dominating source F1 is not coincident with the peak of the molecular line emission of the hot molecular core. Instead, it is displaced by ~1.7 arcsecs, which translates to roughly 10 000 AU on a linear scale. We estimate that the second object F2 is probably a foreground star not intrinsically related to the star-forming region. No reliable interpretation can be given for the third very faint object F3 in the HMC region, since it is only visible in the K_s and L' band.
2.) Very near the peak of the HMC molecular line emission and partly blended with the foreground star we find faint diffuse emission at 2.16 μm. While the foreground star F2 quickly fades at wavelengths >3 μm, this emission strongly increases in the thermal infrared and finally reveals the presence of another object, F4. We propose that object F4 is directly associated with the HMC. This presents the first detection of a hot molecular core at a wavelength as short as 3.8 μm. We know that the HMC probably drives a molecular outflow roughly aligned with the line of sight (Hofner et al. 2001). Thus, the clearing effect of this outflow might allow us to look deeper into the infrared-emitting regions of the core environment. The results of our *K* band polarimetry support the interpretation that the diffuse *K* band emission arises from scattering of light in the outflow cone. Finally, our mid-infrared data highlight object F4 as the most luminous object within the HMC region. With the SED of F4 the range for several parameters of the HMC can be narrowed.
3.) The combined results of the astrometry and radiative transfer computations make it unlikely that the dominant object F1 is a direct trace of the HMC. Nevertheless, we have demonstrated that on the basis of the NIR colours and the *K* band spectrum the most likely explanation is a dense dust shell around a deeply embedded object of lower

luminosity. This might be a hint for multiplicity of YSOs within the HMC region. In a way, G9.62+0.19-F resembles the Orion Hot Core region, where likewise the near vicinity of the HMC is populated by a variety of infrared sources.

4.) We evalute the fact that the UCHIIs D and E are not detected in our infrared data although these objects show much stronger radio emission than the HMC region F. By reexamining available high-resolution radio molecular line data we derive theoretical values for the extinction towards D and E and show that our non-detections are in agreement with these predictions.

5.) Using our *K*-narrow-band results and the imaging polarimetry we reveal within the whole G9.62+0.19 star-forming complex well-defined regions of enhanced Brγ and H_2 emission as well as a sector where a large contribution comes from scattered light. This demonstrates the complex composition of such high-mass star-formation regions that would escape our views when just using simple broad-band imaging.

6.) Generally, we come to the following conclusions. The infrared appearance of complex star forming regions is not exclusively governed by the intrinsic spectral energy distribution of the YSOs but often dominated by the distribution and asymmetries of the extincting circumstellar material on several scales. The interaction of outflows from YSOs with their surroundings can lead to more complicated configurations. In particular, infrared emission associated with HMCs is detectable under certain favourable circumstances, as we demonstrated for G9.62+0.19–F.

While spatial low-resolution data, e.g., from the previous generation of IR satellites, could act as a principle guide line for investigating massive star formation, high-resolution observations are an essential tool for disentangling the objects in high-mass star-forming regions and for making any fundamental progress in that field. For this, accurate astrometry is needed since it can have a strong impact on the interpretation of the data.

Acknowledgements. We thank L. Testi for providing the SOFI *K* band spectrum, M. Rubio and A. Watson for helpful advice, and J. De Buizer for some stimulating discussions during two conference occasions. We especially thank our referee, Dr. Riccardo Cesaroni for a constructive report that focused the paper on some critical points where the referee seemed to have more confidence in our work than we had. The work of H.L. and B.S. was supported by the German *Deutsche Forschungsgemeinschaft, DFG* project numbers Ste 605/17–1 and 605/17–2. P.H. acknowledges the partial support from the Research Corporation grant Nr. CC4996, as well as from NSF grant AST-0098524. This research has made extensive use of the *ALADIN* interactive sky atlas (Bonnarel et al. 2000) and the *VIZIER* catalogues (Ochsenbein et al. 2000), both provided by *CDS*, Strasbourg, France. Furthermore, we used NASA's Astrophysics Data System (ADS) for accessing the literature listed in the references.
This research made use of data products from the Midcourse Space Experiment (*MSX*) and of the NASA/IPAC Infrared Science Archive, which is operated by the Jet Propulsion Laboratory, California Institute of Technology, under contract with the National Aeronautics and Space Administration.

References

Altenhoff, W., Mezger, P. G., Wendker, H., & Westerhout, G. 1960, Veröff. Sternwarte Bonn, 59, 48
André, P., Ward-Thompson, D., & Barsony, M. 1993, ApJ, 406, 122
Apai, D., Linz, H., Stecklum, B., & Henning, Th. 2005, A&A, accepted
Araya, E., Hofner, P., Churchwell, E., & Kurtz, S. 2002, ApJS, 138, 63
Beckert, Th., Duschl, W. J., & Mezger, P. G. 2000, A&A, 356, 1149
Beckwith, S. V. W., & Sargent, A. I. 1991, ApJ, 381, 250
Beckwith, S. V. W., Henning, Th., & Nakagawa, Y. 2000, in Protostars & Planets IV, ed. V. Mannings, A. Boss, & S. Russel (University of Arizona Press), 299
Bessell, M. S., & Brett, J. M. 1988, PASP, 100, 1134
Bertero, M., Boccacci, P., & Robberto, M. 2000, PASP, 112, 1021 (BBR)
Bieging, J. H., Rieke, M. J., & Rieke, G. H. 2002, A&A, 384, 965
Black, J. H., & van Dishoeck, E. F. 1987, ApJ, 322, 412
Bonnarel, F., Fernique, P., Bienaymé, O., et al. 2000, A&AS, 143, 33
Cesaroni, R., Churchwell, E., Hofner, P., Walmsley, C. M., & Kurtz, S. 1994, A&A, 288, 903
Cesaroni, R., Hofner, P., Walmsley, C. M., & Churchwell, E. 1998, A&A, 331, 331
Cutri, R. M., Skrutskie, M. F., van Dyk, S., et al. 2003, 2MASS All-Sky Catalog of Point Sources, VizieR On-line Data Catalog: II/246, originally published in: University of Massachusetts and Infrared Processing and Analysis Center
D'Alessio, P., Calvet, N., & Hartmann, L. 2001, ApJ, 553, 321
De Buizer, J. M., Piña, R. K., & Telesco, C. M. 2000, ApJS, 130, 437
De Buizer, J. M., Watson, A. M., Radomski, J. T., Piña, R. K., & Telesco, C. M. 2002, ApJ, 564, L101
De Buizer, J. M., Radomski, J. T., Telesco, C. M., & Piña, R. K. 2003, ApJ, 598, 1127
Dorschner, J., Begemann, B., Henning, T., Jäger, C., & Mutschke, H. 1995, A&A, 300, 503
Dougados, C., Léna, P., Ridgway, S. T., Christou, J C., & Probst, R. G. 1993, ApJ, 406, 112
Downes, D., Wilson, T. L., Bieging, J., & Wink, J. 1980, ApJS, 40, 379
Draine, B. T., & Lee, H. M. 1984, ApJ, 285, 89
Draine, B. T., & Bertoldi, F. 1996, ApJ, 468, 269
Egan, M. P., & Price, S. D. 1996, AJ, 112, 2862
Egan, M. P., Shipman, R. F., Price, S. D., et al. 1998, ApJ, 494, L199
Epchtein, N., Deul, E., Derriere, S., et al. 1999, A&A, 349, 236
Feldt, M., Stecklum, B., Henning, Th., et al. 1998, A&A, 339, 759
Feldt, M., Stecklum, B., Henning, Th., Launhardt, R., & Hayward, T. L. 1999, A&A, 346, 243
Fernandes, A., Brand, P. W. J. L., & Burton, M. 1995, Ap&SS, 233, 45
Fischer, O., Henning, Th., & Yorke, H. W. 1996, A&A, 308, 863
Garay, G., & Lizano, S. 1999, PASP, 111, 1049
Garay, G., Rodriguez, L. F., Moran, J. M., & Churchwell, E. 1993, ApJ, 418, 368
Gaume, R. A., Claussen, M. J., de Pree, C. G., Goss, W. M., & Mehringer, D. M. 1995, ApJ, 449, 663
Gezari, D. Y., Backman, D. E., & Werner, M. W. 1998, ApJ, 509, 283
Gezari, D. Y., Danchi, W. C., Greenhill, L. J., & Varosi, F. 2003, IAU Symp., 221, ed. M. G. Burton, R. Jayawardhana, & T. L. Bourke, E212
Grady, C. A., Woodgate, B., Torres, C. A. O., et al. 2004, ApJ, 608, 809
Guibert, J. 1992, in Proc. of the Conference on Digitised Optical Sky Surveys, ed. H. T. MacGillivray, & E. B. Thomson (Dordrecht: Kluwer), 103

Hartmann, L. 2003, ApJ, 585, 398
Hayward, T. L., Miles, J. W., Houck, J. R., Gull, G. E., & Schoenwald, J. 1993, Proc. SPIE, 1946, 334
Henning, Th., Feldt, M., & Stecklum, B. 2002, in Hot Star Workshop III: The earliest stages of massive star birth, ed. P. A. Crowther, ASP Conf. Ser., 267, 153
Hofner, P., & Churchwell, E. 1996, A&AS, 120, 283
Hofner, P., Kurtz, S., Churchwell, E., Walmsley, C. M., & Cesaroni, R. 1994, ApJ, 429, L85
Hofner, P., Kurtz, S., Churchwell, E., Walmsley, C. M., & Cesaroni, R. 1996, ApJ, 460, 359
Hofner, P., Wiesemeyer, H., & Henning, Th. 2001, ApJ, 549, 425
Hummer, D. G., & Storey, P. J. 1987, MNRAS, 224, 801
Kaufman, M. J., Hollenbach, D. J., & Tielens, A. G. G. M. 1998, ApJ, 497, 276
Kim, K.-T., & Koo, B.-C. 2003, ApJ, 596, 362
Kurtz, S. E., Churchwell, E., & Wood, D. O. S. 1994, ApJS, 91, 659
Kurtz, S., Cesaroni, R., Churchwell, E., Hofner, P., & Walmsley, C. M. 2000, in Protostars & Planets IV, ed. V. Mannings, A. Boss, & S. Russel (University of Arizona Press), 299
Kurtz, S. E. 2000, Rev. Mex. Astron. Astrofis., 9, 169
Lasker, B., Sturch, C. H., McLean, B. J., et al. 1990, AJ, 99, 2019
Linz, H., Stecklum, B., Henning, Th., et al. 2004, A&A, in preparation
Liu, S.-Y. 2003, IAU Symp., 221, ed. M. G. Burton, R. Jayawardhana, & T. L. Bourke, E233
Lockman, F. J. 1989, ApJS, 71, 469
McCabe, C., Duchene, G., & Ghez, A. M. 2003, ApJ, 588, L
McCartney, M. S. K., Brand, P. W. J. L., Burton, M. G., & Chrysostomou, A. 1999, MNRAS, 307, 315
Manske, V., & Henning, Th. 1998, A&A, 337, 85
Mathis, J. S. 1990, ARA&A, 28, 37
Mathis, J. S., Rumpl, W., & Nordsieck, K. H. 1977, ApJ, 217, 425
Mezger, P. G., & Henderson, A. P. 1967, ApJ, 147, 471
Minchin, N. R., Hough, J. H., McCall, A., et al. 1991, MNRAS, 248, 715
Minier, V., Booth, R. S., Ellingsen, S. P., Conway, J. E., & Pestalozzi, M. R. 2001, in Proc. of the 5th EVN Symposion, ed. J. E. Conway, A. G. Polatidis, R. S. Booth, & Y. Pihlstroem, 178
Moorwood, A. F. 1997, in Proc. SPIE, 2871, ed. A. L. Ardeberg, 1146
Monet, D., Bird, A., Canzian, B., et al. 1998: USNO-A V2.0, A Catalog of Astrometric Standards, U.S. Naval Observatory Flagstaff Station (USNOFS) and Universities Space Research Association (USRA) stationed at USNOFS
Ochsenbein, F., Bauer, P., & Marcout, J. 2000, A&AS, 143, 221
Osorio, M., Lizano, S., & D'Alessio, P. 1999, ApJ, 528, 808
Ossenkopf, V., & Henning, Th. 1994, A&A, 291, 943
Osterbrock, D. E. 1989, Astrophysics of Gaseous Nebulae and Active Galactic Nuclei, University of Science Books, Sausalito, California
Pantin, E., & Starck, J.-L. 1996, A&AS, 118, 575
Pascucci, I., Apai, D., Henning, Th., Stecklum, B., & Brandl, B. 2004, A&A, 426, 523
Peeters, E., Martín-Hernández, N. L., Damour, F., et al. 2002a, A&A, 381, 571
Peeters, E., Hony, S., Van Kerckhoven, C., et al. 2002b, A&A, 390, 1089
Persi, P., Tapia, M., Roth, M., et al. 2003, A&A, 397, 227
Persson, S. E., Murphy, D. C., Krzeminski, W., Roth, M., & Rieke, M. J. 1998, AJ, 116, 2475
Phillips, C. J., Norris, R. P., Ellingsen, S. P., & McCulloch, P. M. 1998, MNRAS, 300, 1131
Preibisch, Th., Ossenkopf, V., Yorke, H. W., & Henning, Th. 1993, A&A, 279, 577
Ramírez, S. V., Depoy, D. L., Frogel, J. A., Sellgren, K., & Blum, R. D. 1997, AJ, 113, 1411
Reimann, H.-G., Linz, H., Wagner, R., et al. 2000, in Proc. SPIE, 4008, ed. M. Iye, & A. F. Moorwood, 1132
Rodgers, S. D., & Charnley, S. B. 2001, ApJ, 546, 324
Rodgers, S. D., & Charnley, S. B. 2003, ApJ, 585, 355
Rouan, D., & Leger, A. 1984, A&A, 132, L1
Ryter, Ch. E. 1996, Ap&SS, 236, 285
Schlegel, D. J., Finkbeiner, D. B., & Davis, M. 1998, ApJ, 500, 525
Schreyer, K., Henning, Th., Kömpe, C., & Harjunpää, P. 1996, A&A, 306, 267
Schreyer, K., Stecklum, B., Linz, H., & Henning, Th. 2003, ApJ, 599, 335
Serkowski, K. 1962, Advances in Astronomy and Astrophysics, 1, 289
Shu, F. H., Adams, F. C., & Lizano, S. 1987, ARA&A, 25, 23
Shuping, R. Y., Bally, J., Morris, M., & Throop, H. 2003, ApJ, 587, L109
Simmons, J. F. L., & Stewart, B. G. 1985, A&A, 142, 100
Stahler, S. W., Palla, F., & Ho, P. T. P. 2000, in Protostars & Planets IV, ed. V. Mannings, A. Boss, & S. Russel (University of Arizona Press), 327
Stecklum, B., Brandl, B., Feldt, M., et al. 2001, in The Origins of Stars and Planets – The VLT View., ed. J. Alves, & M. McCaughrean, ESO Astrophysics Symposia, 225
Stecklum, B., Brandl, B., Feldt, M., Henning, Th., & Pascucci, I. 2002, A&A, 392, 1025
Stecklum, B., Feldt, M., Henning, Th., Käufl, H. U., & Wolf, S. 2003, in Galactic Star Formation Across the Stellar Mass Spectrum, ed. J. De Buizer, ASP Conf. Ser., 287 [arXiv:astro-ph/0206457]
Stecklum, B., Henning, Th., Apai, D., & Linz, H. 2003, in Proc. SPIE, 4834, ed. G. Guhathakurta, 337
Tamura, M., Gatley, I., & Joyce, R. R., et al. 1991, ApJ, 378, 611
Tenorio-Tagle, G. 1979, A&A, 71, 59
Testi, L., Felli, M., Persi, P., & Roth, M. 1998, A&A, 329, 233
Testi, L., Hofner, P., Kurtz, S., & Rupen, M. 2000, A&A, 359, L5
Testi, L. 2001, private communication
Tieftrunk, A. R., Gaume, R. A., Claussen, M. J., Wilson, T. L., & Johnston, K. J. 1997, A&A, 318, 931
Urban, S. E., Corbin, T. E., & Wycoff, G. L. 1997, The ACT Reference Catalogue, US Naval Observatory, Washington DC
van der Bliek, N. S., Manfroid, J., & Bouchet, P. 1996, A&AS, 119, 547
Walsh, A. J., Burton, M. G., Hyland, A. R., & Robinson, G. 1999, MNRAS, 309, 905
Wardle, J. F. C., & Kronberg, P. P. 1974, ApJ, 194, 249
Watson, A. M., Coil, A. L., Shepherd, D. S., Hofner, P., & Churchwell, E. 1997, ApJ, 487, 818
Wegner, W. 1994, MNRAS, 270, 229
Weintraub, D. A., & Kastner, J. 1993, ApJ, 411, 767
Wolf, S., Henning, Th., & Stecklum, B. 1999, A&A, 349, 839
Wood, D. O. S., & Churchwell, E. 1989, ApJS, 69, 831
Yao, Y., Hirata, N., Ishii, M., et al. 1997, ApJ, 490, 281
Yao, Y., Ishii, M., Nagata, T., Nakaya, H., & Sato, S. 2000, ApJ, 542, 392
Yorke, H. W. 1980, A&A, 85, 215
Yorke, H. W., & Shustov, B. M. 1981, A&A, 98, 125
Yorke, H. W. 1986, ARA&A, 24, 49
Yorke, H. W. 2003, IAU Symp., 221, ed. M. G. Burton, R. Jayawardhana, & T. L. Bourke, E108

Online Material

Appendix A: NIR astrometry

Special care was taken to establish accurate astrometry for the *VLT* NIR data. Two approaches were used:

- first, we extracted an *I*-band image from the *ALADIN* interactive sky atlas (Bonnarel et al. 2000) that contained the region of interest. The image we used had been constructed by digital scanning of a *SERC*–I photo plate, using the *MAMA/CAI* scanning facility (Guibert 1992). Such an image has – in comparison to *DSS1* and *DSS2* images – a smaller pixel scale (0.″67/px). Within this (11.′5 × 11.′5) subimage we found three useful stars also included in the *ACT* reference catalogue (Urban et al. 1997). We calibrated the *I*-band image with the help of these *ACT* stars and used this image as an astrometric reference to adjust the *VLT*–K_s image. This could be done straightforwardly since many stars in the central region of the *I*-band image were also present in the *VLT* image;
- the second way was more direct without an intermediate step. By applying the *ALADIN* tool we identified more than ten stars in our *VLT* image also included in the *USNO-A2.0* catalogue (Monet et al. 1998)[13]. We then used these catalogued stellar positions to directly calibrate the *VLT* image. Nevertheless, one has to be careful when choosing these stars. Some objects which, due to the lower resolution, seem to be star-like on the optical plate images and are therefore included in star catalogues like *USNO-A2.0*, turn out to be stars with associated nebulosity or clusters of stars when imaged with high resolution. Hence, we checked our selection of stars by examining publicly available digitised images of the region. Only positions which appeared to be clearly associated with one single object in both the optical and the NIR images have been used for the calibration.

The two methods gave almost identical results. A comparison of several object positions resulted in deviations of ≤0.″25 between the two methods.

After applying these astrometrical calibrations the "red" compact object F1 is still 1.7 arcsec away from the position of radio component F – a discrepancy which we find to be significant regarding the high resolution of the data. Furthermore, we should mention that the positional difference between our astrometry and the one in Testi et al. (1998) is obvious, but not large. On the other hand, there is a substantial astrometric disagreement between our newly derived positions and the ones given in Walsh et al. (1999) for their *K* band image of the G9.62+0.19 region.

[13] We used the USNO-A2.0 catalogue because it is more or less directly tied to the HIPPARCOS reference frame. In the meantime, we also checked the astrometry for the G9.62+0.19 region according to the 2MASS All Sky Survey (Cutri et al. 2003). An offset of around 0.3 arcsec seems to exist between the two catalogues for G9.62+0.19. We can and will not evaluate here which catalogue is more accurate. We just mention that the 2MASS astrometry places our object F4 even closer (0.″15) to the peak of the HMC molecular line emission (see Fig. 4).

For their investigations of G9.62+0.19 Persi et al. (2003) use the (preliminary) *DENIS* point source catalogue (Epchtein et al. 1999) as astrometric reference. This choice is problematic since this catalogue itself uses the old (pre–*HIPPARCOS*) Guide Star Catalog GSC 1 (Lasker et al. 1990) for calibration. As a test, we looked for stars in our VLT images which are included in USNO2 as well as in *DENIS*. Simple marking of the coordinates given in the catalogues reveals that all *DENIS* positions seem to be systematically shifted ≈2.5 arcsec to the north-northwest. From that spot check we cannot assert a global problem for the astrometry of the *DENIS* catalogue. But it is obvious that the particular strip of the *DENIS* release data which contains the G9.62+0.19 region suffers from imprecise astrometry and should not be used for calibrating high-resolution data.

Appendix B: Correct position of the compact MIR emission in G9.62+0.19–F

De Buizer et al. (2000) first reported on this MIR feature. They used previous 23 GHz continuum data (Cesaroni et al. 1994) to correlate their MIR data. These radio data did not yet reveal the presence of the weak 1.3 cm radio emission arising from component F, but only showed the peak belonging to component D (cf. the overlaid contours in Fig. 5). They then assumed that this radio continuum peak for D should be coincident with the MIR peak. However, more recent investigations could already show that the compact mid-IR source does not coincide with radio component D (see Stecklum et al. 2001; Persi et al. 2003). Both groups placed the emission within the HMC region G9.62+0.19–F. The astrometry was mainly based on the comparison of centroids of the extended emission (component B) from the science data and from the (coarser) 12.1 μm *MSX* images showing the same field. Still, the error of such a method is around 2″ and does not make it possible to decide to which of the objects in the HMC region the MIR compact emission is related. Finally, De Buizer et al. (2003) presented new 11.7 μm data that seem to show that the MIR emission is associated neither with component D nor with component F but is displaced from both by roughly 2–3 arcsec. Their new astrometry is based on a correlation between MIR features and a 3.5 cm ATCA interferometric radio map taken from Phillips et al. (1998).

In an attempt to clarify the situation, we observed G9.62+0.19 at 8.7 μm (*N*1 filter), using TIMMI2. The smaller wavelength (compared to 11.7 μm) and the larger field of view (compared to SpectroCam-10) should facilitate the search for compact reference objects in the field. The result is shown in Fig. 6, where we overlay the TIMMI2 data on our NIR data. In the north we found a bright star, also visible in the K_s, L', and M band, suitable for linking the TIMMI2 astrometry to the VLT astrometry. The small rotation misalignment of the TIMMI2 chip with respect to the sky coordinate system could be estimated independently, because during the observating run we also observed other regions that showed several sources with 2MASS counterparts in the field of view (Grady et al. 2004; Linz et al. 2004). The positional uncertainty is around 0.4 arcsecs in RA and Dec (i.e. 2 pixels in each direction). We cannot confirm the astrometric result of De Buizer et al. (2003). We find that the compact MIR emission is indeed located in

the direct vicinity of the HMC. Our astrometry speaks against a straight identification of the compact MIR emission with object F1, but rather suggests that the peak of the MIR emission is closer to object F4. In comparison to the 11.7 μm data, the MIR emission blob is not pointlike. We therefore deconvolved this part of the image using the standard star HD 169916 as PSF reference. The result (cf. in Fig. 4) is an elongated structure with a similar position angle (55° ± 6°) as the F1–F4 object pair (51.5° ± 2°). This further strengthens our diagnosis that also at 8.7 μm do we see the objects F4 and F1 that seem to merge into one object due to the lower spatial resolution of the TIMMI2 data. The relative strengths of the contributions of the two objects are governed by the very different spectral energy distributions of F1 and F4 (see Fig. 9).

We should finally mention that one fraction of the astrometrical disagreement between De Buizer et al. (2003) and our result disappears when an agreement is reached about the exact radio reference position for the HMC! We note that they use the J2000 position $18^{\rm h}06^{\rm m}14\overset{\rm s}{.}82$ (RA), $-20°31'38\overset{''}{.}4$ (Dec) as HMC reference position (cf. their Table 1 and their Fig. 2). But this corresponds neither to the peak of the $NH_3(5, 5)$ emission nor to the position of the faint 3.6 cm continuum of the HMC (see our Table 2 or consult the respective references therein). The difference between the 3.6 cm peak position, which we use as HMC position throughout this paper and which is the most accurate position for this hot core to date, and the De Buizer values is ca. 0.85 arcsec in RA and ca. 1.0 arcsec in Dec, the total displacement is hence around 1.3 arcsec. Taking this into account the disagreement between De Buizer's and our estimation still does not vanish completely, but has shrunk considerably.

Appendix C: MIR image restoration

If, due to the necessary chopping and nodding in the MIR, one has the positive and negative beams in the final image the usual way to treat the data is to perform a shift and add. However, in principle it is possible to deconvolve the image using a matrix multiplication procedure. We refer to Bertero et al. (2000, hereafter BBR) for details of this so-called projected Landweber method. The basic idea is that within the final multi-beam image several points at different sky positions contribute to the signal contained in one pixel of the detector array. Assuming that the chopping and nodding throws are colinear along the vertical orientation of the detector chip one can describe the multi-beam image $\boldsymbol{g}$ as result of a multiplication of the actually mapped larger rectangular field $\boldsymbol{f}$ with a simple imaging matrix $\mathbf{A}$, populated just with natural numbers (see BBR):

$$g = \mathrm{A}\, f. \tag{C.1}$$

The projected Landweber method deals with this inversion problem to restore the original field $\boldsymbol{f}$. The following iterative ansatz is used:

$$f^{(\mathrm{k}+1)} = \mathrm{P}_+ \left[f^{(\mathrm{k})} + \tau \left(\mathrm{A}^{\mathrm{T}} g - \mathrm{A}^{\mathrm{T}} \mathrm{A} f^{(\mathrm{k})} \right) \right]. \tag{C.2}$$

Here P_+ is the projection onto the positive subset of iterative solutions, $\mathbf{A}^{\mathrm{T}}$ is the transposed matrix, and τ is a relaxation parameter that is related to the largest singular value of the matrix $\mathbf{A}$. As starting point $\boldsymbol{f}^{(0)} = \mathbf{0}$ is chosen.

Applying this method, some effects can influence the quality of the restoration. This concerns the appearance of ghost images of the restored objects at distances that are multiples of the chopping/nodding throws. Such artefacts are inherent in the method itself and can be understood mathematically. The BBR article deals with techniques for reducing/removing several kinds of artefacts that may appear.

Since we used for our observations a chop-nod pattern different from the one used in the BBR approach (chopping perpendicular to nodding vs. chopping parallel to nodding), we had to adapt the original version of their program. Due to the loss of colinearity the problem now is really a two-dimensional one; thus, one imaging matrix is not sufficient. The new imaging equation now reads, with two imaging matrices $\mathbf{A}$ and $\mathbf{B}$:

$$g = \mathrm{A}\, f\, \mathrm{B}. \tag{C.3}$$

The iteration equation evolves to the new key formula:

$$f^{(\mathrm{k}+1)} = \mathrm{P}_+ \left[f^{(\mathrm{k})} + \tau \left(\mathrm{A}^{\mathrm{T}} g\, \mathrm{B}^{\mathrm{T}} - \mathrm{A}^{\mathrm{T}} \mathrm{A}\, f^{(\mathrm{k})}\, \mathrm{B}\, \mathrm{B}^{\mathrm{T}} \right) \right]. \tag{C.4}$$

In principle, there is good reason to apply such a restoration method. First, one can easily disentangle the regions in the multi-beam image where positive and negative components overlap when imaging crowded fields. In this regard, our approach has already proven to be effective for the case of TIMMI2 imaging of NGC 2264 IRS1 (Schreyer et al. 2003). Second, one gains a larger field of view, because the reconstructed image covers the areas of both the on-beams and the off-beams. This is of course an advantage when one tries to map extended objects with the medium-sized (not to say small) MIR detector arrays available nowadays. In addition, within a larger field it might also be easier to find other objects that could serve as astrometric reference points.